HAL open science

Rheological change and degassing during a trachytic Vulcanian eruption at Kilian Volcano, Chaîne des Puys, France

Mathieu Colombier, Thomas Shea, Alain Burgisser, Timothy Druitt, Lucia Gurioli, Dirk Müller, Francisco Cáceres, Kai-Uwe Hess, Pierre Boivin, Didier Miallier, et al.

To cite this version:

Mathieu Colombier, Thomas Shea, Alain Burgisser, Timothy Druitt, Lucia Gurioli, et al.. Rheological change and degassing during a trachytic Vulcanian eruption at Kilian Volcano, Chaîne des Puys, France. Bulletin of Volcanology, 2020, 82, pp.78. 10.1007/s00445-020-01420-5 . hal-03015892v2

HAL Id: hal-03015892

https://uca.hal.science/hal-03015892v2

Submitted on 25 Nov 2020

HAL is a multi-disciplinary open access archive for the deposit and dissemination of scientific research documents, whether they are published or not. The documents may come from teaching and research institutions in France or abroad, or from public or private research centers.

L'archive ouverte pluridisciplinaire **HAL**, est destinée au dépôt et à la diffusion de documents scientifiques de niveau recherche, publiés ou non, émanant des établissements d'enseignement et de recherche français ou étrangers, des laboratoires publics ou privés.

Distributed under a Creative Commons Attribution 4.0 International License

Bulletin of Volcanology (2020) 82:78
https://doi.org/10.1007/s00445-020-01420-5

RESEARCH ARTICLE

Rheological change and degassing during a trachytic Vulcanian eruption at Kilian Volcano, Chaîne des Puys, France

Mathieu Colombier[1] · Thomas Shea[2] · Alain Burgisser[3] · Timothy H. Druitt[4] · Lucia Gurioli[4] · Dirk Müller[1] · Francisco Cáceres[1] · Kai-Uwe Hess[1] · Pierre Boivin[4] · Didier Miallier[5] · Donald B. Dingwell[1]

Received: 17 March 2020 / Accepted: 4 November 2020
© The Author(s) 2020

Abstract

Magma ascent during silicic dome-forming eruptions is characterized by significant changes in magma viscosity, permeability, and gas overpressure in the conduit. These changes depend on a set of parameters such as ascent rate, outgassing and crystallization efficiency, and magma viscosity, which in turn may influence the prevailing conditions for effusive versus explosive activity. Here, we combine chemical and textural analyses of tephra with viscosity models to provide a better understanding of the effusive-explosive transitions during Vulcanian phases of the 9.4 ka eruption of Kilian Volcano, Chaîne des Puys, France. Our results suggest that effusive activity at the onset of Vulcanian episodes at Kilian Volcano was promoted by (i) rapid ascent of initially crystal-poor and volatile-rich trachytic magma, (ii) a substantial bulk and melt viscosity increase driven by extensive volatile loss and crystallization, and (iii) efficient degassing/outgassing in a crystal-rich magma at shallow depths. Trachytic magma repeatedly replenished the upper conduit, and variations in the amount of decompression and cooling caused vertical textural stratification, leading to variable degrees of crystallization and outgassing. Outgassing promoted effusive dome growth and occurred via gas percolation through large interconnected vesicles, fractures, and tuffisite veins, fostering the formation of cristobalite in the carapace and talus regions. Build-up of overpressure was likely caused by closing of pore space (bubbles and fractures) in the dome through a combination of pore collapse, cristobalite formation, sintering in tuffisite veins, and limited pre-fragmentation coalescence in the dome or underlying hot vesicular magma. Sealing of the carapace may have caused a transition from open- to closed- system degassing and to renewed explosive activity. We generalize our findings to propose that the broad spectrum of eruptive styles for trachytic magmas may be inherited from a combination of characteristics of trachytic melts that include high water solubility and diffusivity, rapid microlite growth, and low melt viscosity compared to their more evolved subalkaline dacitic and rhyolitic equivalents. We show that trachytes may erupt with a similar style (e.g., Vulcanian) but at significantly higher ascent rates than their andesitic, dacitic, and rhyolitic counterparts. This suggests that the periodicity of effusive-explosive transitions at trachytic volcanoes may differ from that observed at the well-monitored andesitic, dacitic, and rhyolitic volcanoes, which has implications for hazard assessment associated with trachytic eruptions.

Keywords Effusive-explosive transitions · Trachytic magma · Vulcanian eruption · Magma Viscosity · Crystallization · Degassing · Nanolites · Cristobalite

Editorial responsibility: M.R. James; Deputy Executive Editor: J. Tadeucci

✉ Mathieu Colombier
mathieu.colombier@min.uni-muenchen.de

[1] Department of Earth and Environmental Sciences, Ludwig-Maximilians-Universität, München, Germany

[2] Geology and Geophysics, University of Hawai'i at Mānoa, Honolulu, HI, USA

[3] Univ. Savoie Mont Blanc, CNRS, IRD, ISTerre, F-73376 Le Bourget du Lac, France

[4] Université Clermont Auvergne -CNRS-IRD, OPGC, Laboratoire Magmas et Volcans, F-63100 Clermont-Ferrand, France

[5] Université Clermont Auvergne, CNRS–IN2P3, LPC, F-63000 Clermont-Ferrand, France

Published online: 20 November 2020

Introduction

Understanding and forecasting effusive-explosive transitions during intermediate-to-silicic volcanic eruptions is a key objective of volcanology. Such transitions occur frequently (Cassidy et al. 2018), yet they remain difficult to anticipate. Shifts between effusive and explosive phases at a given volcano can occur at different timescales, either between several eruptions or within single eruptive periods (Cassidy et al. 2018). We focus hereafter on this second scenario of rapid and repeated effusive-explosive transitions during single events of Vulcanian eruptions. During andesitic, dacitic, and trachytic eruptions, effusive phases commonly lead to the emplacement of crystal-rich lava domes or plugs stalling at shallow levels of the conduit (Platz et al. 2007; Lavallée et al. 2012; Kushnir et al. 2016; Colombier et al. 2017a; Heap et al. 2018). Explosive activity and conduit evacuation can in turn be triggered by the pressurization of underlying vesicular magma, which ultimately yields a downward propagation of a fragmentation front within the conduit (e.g., Druitt et al. 2002; Platz et al. 2007; Giachetti et al. 2010; Calder et al. 2015), or by over-pressurization of the dome itself (Boudon et al. 2015). As a result of these transitions, dense, crystal-rich, dome-derived pyroclasts and highly vesicular, conduit-derived pumice pyroclasts commonly coexist in the deposits of Vulcanian eruptions leading to bimodal porosity/density distributions of the pyroclasts (Formenti and Druitt 2003; Adams et al. 2006; Mujin and Nakamura 2014; Colombier et al. 2017a). Crystallization during magma ascent and stagnation at shallow levels, is mostly driven by processes related to decompression, degassing, and/or cooling (e.g., Blundy and Cashman 2001; Arzilli and Carroll 2013; Zorn et al. 2018).

Effusive-explosive transitions have been proposed to arise from differences in magma ascent rate (Platz et al. 2007; Cassidy et al. 2018), degassing conditions (Eichelberger et al. 1986; Jaupart and Allègre 1991), pre- or syn-eruptive volatile content (Andújar and Scaillet 2012; Forte and Castro 2019), rheological changes in the magma (Moitra et al. 2018; Cassidy et al. 2018), and lava-water interaction (Belousov et al. 2011; Fitch et al. 2017). The emplacement of lava domes is typically associated with significant gas loss from the magma by outgassing through connected bubble networks, fractures, or intergranular pore space (Kendrick et al. 2016; Colombier et al. 2017b; Lamur et al. 2017; Yoshimura et al. 2019). Magma permeability is the dominant factor controlling the ability of gas to escape from the magma, and its evolution is both complex and highly transient in lava domes (Mueller et al. 2005). Rheological changes in the lava dome also have an important role in controlling cyclic and hybrid eruptive style (Lavallée et al. 2013). They are principally governed by the kinetics of crystallization, bubble nucleation and growth, and variations in volatile content and temperature (cooling or heating). All these processes may have competing effects on eruptive style. As an example, an increase in magma viscosity may (1) lead to a slower ascent rate, which in turn may promote gas escape, magma cooling, and effusive activity, or (2) have the opposite effect of causing gas overpressure and magma brittle fragmentation, leading to explosive eruption. Finally, ascent rate controls the time available for the formation of a permeable magma. Faster ascent rates offer less time for permeable gas pathways to develop, thereby favoring explosive activity (Cassidy et al. 2018).

Trachytic (and phonolitic) silicate melts differ strongly from their more widespread, subalkaline counterparts (andesites, dacites, and rhyolites) in several ways. Firstly, they have lower viscosities at similar conditions of SiO_2 content, temperatures, and dissolved H_2O than rhyolitic melts due to differences in melt compositions (Andújar and Scaillet 2012). Secondly, trachytic melts are inferred to crystallize faster than subalkaline compositions, with higher crystal nucleation and growth rates leading to higher crystallinities and crystal number densities on a given timescale (Arzilli and Carroll 2013; Shea et al. 2017). As crystals are known to promote permeable gas escape at lower porosities (e.g., Blower 2001; Oppenheimer et al. 2015; Colombier et al. 2017b; Lindoo et al. 2017; Colombier et al. 2020), one might expect that the timing and efficiency of outgassing are strongly influenced by the high rates of crystallization experienced by trachytic magmas during ascent. Such rapid crystallization may also promote heterogenous bubble nucleation on crystals (Cluzel et al. 2008), thereby reducing volatile supersaturation pressure and promoting earlier degassing in the conduit. Additionally, water solubility is higher in trachytic melts than in rhyolites, with water contents exceeding 7 wt% at ~ 200 MPa (Di Matteo et al. 2004; Martel et al. 2013). Depending on the ascent rates of trachytic magmas and the diffusivity of dissolved water, this high water solubility may lead to preservation of high water contents even close to the surface (Di Matteo et al. 2004). On the other hand, slow ascent and high water diffusivity allow magmas to track near-equilibrium water solubility, which is very low at shallow depths (Di Matteo et al. 2004). Fanara et al. (2013) predicted high water diffusivities and therefore more efficient degassing in trachytic melts than in their rhyolitic counterparts at high temperature and high pressures.

In this paper, we combine textural and chemical analysis of pyroclasts from the 9.4 ka trachytic Vulcanian eruption of Kilian Volcano (Colombier et al. 2017a) in order to unravel the mechanisms responsible for effusive-explosive transition during single Vulcanian episodes. This volcano is located in the Chaîne des Puys, a dormant magmatic system approximately 6 km east from the city of Clermont-Ferrand—a proximity which brings with it some concerns regarding volcanic hazards and risk (Delcamp et al. 2014; Latutrie et al. 2016). Constraining the eruptive style of Kilian Volcano is not only a key to unlocking the characteristics of one of the dominant

types of volcanism at the Chaîne des Puys (Martel et al. 2013), but also to improve our understanding of eruptive processes and hazards at monogenetic volcanoes worldwide. More generally, a better understanding of the dynamics behind effusive-explosive transitions is of primary importance to better assess hazards related to cyclic dome-forming eruptions. Although they are less ubiquitous, and commonly less voluminous, than subalkaline magmas, trachytic magmas are often associated with violent explosive volcanic activity (Rosi et al. 1999), and some trachytic volcanoes are located close to highly populated areas (e.g., Campi Flegrei, Italy). Studying the chemical and textural characteristics of products from past trachytic eruptions is essential to identify their eruptive style controls, and to shed light on how they differ from andesitic-rhyolitic magmas.

We propose in what follows that the specific characteristics of trachytic melts such as water solubility, water diffusivity, viscosity, and crystal growth kinetics were likely responsible for rapid changes in magma rheology during the 9.4 ka Kilian eruption and that these rheological changes, coupled with a high outgassing efficiency, exerted a primary control on the kinetics of effusive-explosive transitions at Kilian Volcano. We illustrate how our findings can be extrapolated to other trachytic volcanoes, and show that the degree of crystallization, viscosity, and efficiency of degassing/outgassing are key parameters regulating the eruptive style and cyclicity of trachytic eruptions.

Geological setting

Kilian Volcano is one of several trachytic monogenetic edifices belonging to the Chaîne des Puys, France (Fig. 1). It consists of a crater (enlarged by quarrying) and the partial remains of a lava dome. The Kilian eruption occurred 9.4 ka ago (Miallier et al. 2012) and was characterized by a succession of five eruptive episodes ranging from Vulcanian (dome- or plug-forming) to sub-Plinian (dome- or plug-free) activity, possibly preceded by a phreatic opening phase (Boivin et al. 2017; Colombier et al. 2017a). The reader is referred to Colombier et al. (2017a) for a detailed description of the stratigraphy and related eruptive sequence. Here, we focus on the Vulcanian episodes that have been recently interpreted to result from overpressurization of the hot, vesicular magma column below an outgassed, crystal-rich plug or dome (Colombier et al. 2017a). Despite their different bulk chemical compositions, these Vulcanian explosions and their products shared several similarities with Vulcanian activity at Soufrière Hills volcano in Montserrat, including similar eruptive scenario, pyroclasts density and porosity distributions, and vesicle and crystal textures (Formenti and Druitt 2003; Giachetti et al. 2010; Colombier et al. 2017a).

Proximal tephra deposits from the eruption cover a large part of the Chaîne des Puys, including the top and northern flank of the Puy de Dôme edifice (1450 m a.s.l) located 800 m north-east of Kilian crater (Colombier et al. 2017a; Boivin and Thouret 2014; Portal et al. 2019). A distal tephra layer possibly from Kilian has been identified as far as Soppensee lake in Switzerland (Lane et al. 2011). Van Wyk de Vries et al. (2014) suggested that Kilian crater was created by explosive activity due to the presence of a shallow magmatic intrusion (i.e., cryptodome) on the bulged edifice of Puy Grosmanaux to the south. Kilian crater is partially filled by the remains of a 200-m-wide, 50- to 100-m-thick, trachytic lava dome that creates a positive gravity anomaly (Portal et al. 2016; Boivin et al. 2017). This dome was probably emplaced following the explosive phases.

The samples analyzed in this study are derived from three Vulcanian episodes at Kilian Volcano (Colombier et al. 2017a) and were mainly sampled at the Coupe des Muletiers outcrop located approximately 500 m NE of Kilian crater (Fig. 1). A few additional samples were taken from deposits on the summit of Puy de Dôme volcano, and one in situ dome rock was sampled from the exterior of the dome remnants in Kilian crater (Fig. 1). We note that an additional type of massive trachyte is also associated to Kilian dome although it does not crop out in Kilian crater (Boivin et al. 2015). This lithology has been widely quarried and used for building and ornamental purposes at the Gallo-Roman period and is no longer visible in the crater because it has been covered by quarrying waste and colluvium (Boivin et al. 2015). This peculiar type of trachyte will not be discussed in this study as it is also absent from the tephra deposits and likely represents a late effusive stage.

Methods

Textural, petro-physical, and chemical analysis

Textural observations were made on scanning electron microscope using back-scattered electron images taken on a HITACHI SU 5000 Schottky FE-SEM and electron microprobes at the Ludwig Maximilian University of Munich and at the University of Hawai‘i at Mānoa.

We analyzed the compositions of interstitial glass and microlites in two pumice pyroclasts and six dome pyroclasts using Electron Probe Micro-analysis to complement and complete the preliminary dataset of Colombier et al. (2017a). Glassy areas in some dome pyroclasts were too small to be analyzed. Microprobe analyses at the Ludwig Maximilian University were carried out with a Cameca SX-100 instrument. A 10-μm defocused beam at an accelerating voltage of 15 keV and a current of 5 nA was used in glass analysis in order to limit Na loss. Calibration was done on the

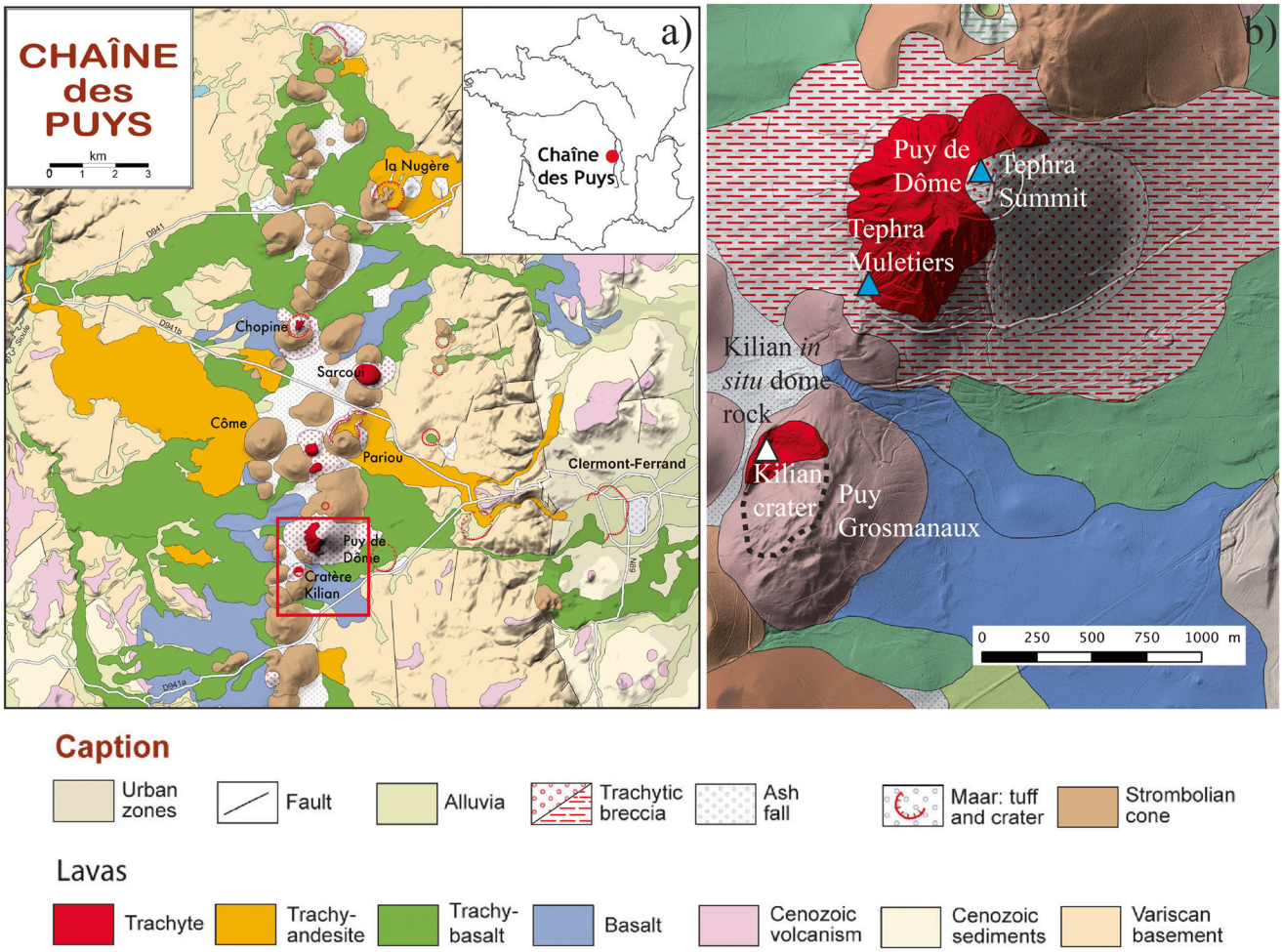

Fig. 1 **a** Map of the Chaîne des Puys with the trachytic domes shown in red. **b** Map showing the locations of samples analyzed in this study. The blue triangles show sites of sampling of the Kilian tephra at the summit of Puy de Dôme lava dome ('Kilian summit') and on the southern flank of Puy de Dôme at the Coupe des Muletiers outcrop ('Kilian Muletiers'). The white triangle in Kilian crater corresponds to an *in situ* dome rock sampled at the exterior of the dome remnants (red area) at the crater rim. The black dashed line delimits the rim Kilian crater

following standards: wollastonite (Ca); albite (Na, Si); periclase (Mg); orthoclase (K, Al); Fe_2O_3 (Fe); Cr_2O_3 (Cr); ilmenite (Ti); bustamite (Mn); apatite (P); vanadinite (Cl); and anhydrite (S). Peak counting time was 10 s for each element (5 s for background on each side of the peak). For matrix correction, the PAP routine, implemented in the Cameca PeakSight software, was used. Another set of analyses was conducted at the University of Hawai'i at Mānoa using a JEOL Field-emission Hyperprobe JXA-8500 device, with an accelerating voltage of 15 kV and a 10-nA beam current. Standards used were VG2 and STG56 glasses (Si, Al, Fe, Ca), Sphene glass (Ti), Verma garnet (Mn), Springwater olivine (Mg), Orthoclase (K), Amelia albite (Na), and Durango apatite (Cl, P). On-peak count times were 20 s (Si, Ti, Na, Fe, K, P, Mn), 30 s (Ca), and 60 s (Cl, Al) with half of those count times off-peak for background measurement. The time-dependent intensity correction implemented in the software Probe for EPMA© was used to track and correct for Na loss and Si gains when needed. Analytical precision was better than 1% relative for Si, Al, Mg, Fe, Ca, 3% relative for Na, K, Ti, 10% relative for P and Cl. Due to the age of the deposits, secondary rehydration by meteoric water caused totals to be lower than 100%. As a result, glasses were normalized to 100% to allow comparison between different pyroclasts but uncorrected raw data are available in the Supplementary Material. Interlaboratory microprobe analysis was carried for practical reasons, and chemical analysis of the same pyroclast measured at the Ludwig Maximilian University of Munich and at the University of Hawai'i at Mānoa yielded similar results. We also performed additional textural analyses and chemical mapping of an in situ dome rock at the scanning electron microscope at the Laboratoire Magmas et Volcans of Clermont-Ferrand.

Eight pumice pyroclasts and five dome pyroclasts were selected for X-ray diffraction (XRD). The finely ground samples were mixed with ~ 17 wt% of silicon (Alfa Aesar Silicon powder, 99.5% purity) as internal standard for quantitative Rietveld refinement. For Rietveld refinement, the software

Profex 3.10.2 (Döbelin and Kleeberg 2015) was used. Measurements were performed with a GE X-ray diffractometer (XRD 3003 TT) in Bragg-Brentano geometry in a 2 theta-range of 10–100 ° by using Cu K_{a1} radiation.

X-ray fluorescence whole rock analyses were carried out on 7 pumice pyroclasts and 4 dome pyroclasts at the Institute of Geosciences, Johannes Gutenberg University Mainz, Germany, using a Philips MagiXPRO device. Loss on ignition was determined after heating the sample for 2 h at 980 °C. The major elements were measured on glass beads, prepared from a mixture of 0.4-g sample powder and 5.2 g $Li_2B_4O_7$.

Petro-physical and chemical data were then used as inputs in SOLVCALC (Wen and Nekvasil 1994) to calculate isotherms in a feldspar ternary diagram and in Rhyolite-MELTS (Gualda et al. 2012) to model crystallization during magma ascent at equilibrium conditions.

The porosity data used in this study were obtained using an immersion technique based on Archimedes principle with negative error bars of 7 vol% corresponding to the maximum difference observed with the glass beads method (showing systematically lower values) for most pyroclasts (Colombier et al. 2017a).

Simultaneous thermal analysis

Two pumice pyroclasts and one dome pyroclast were heated in a STA Netzsch 404C at a heating rate of 10 °C min^{-1} up to 1000 °C to retrieve the glass transition temperature (T_g) and to distinguish between the meteoric and magmatic water contents using thermogravimetric measurement of the mass loss during heating. The error on the glass transition peak is ± 3 °C (Kai-Uwe Hess personal communication).

These results have been combined with porosity, permeability, crystallinity, whole rock and glass analyses, and textural data from our previous study (Table 1; Colombier et al. 2017a).

Results

Classification of pyroclasts based on textural observations

In this study, we mainly focus on pyroclasts from the initial and final Vulcanian phases of the Kilian eruption and include one pyroclast from intermediate sub-Plinian phases (units U1, K1, and K2 in Fig. 3 from Colombier et al. 2017a). For simplicity, we use the same classification as in Colombier et al. (2017a) to distinguish pumice (> 40% porosity) from dense dome-derived pyroclasts (< 40% porosity; hereafter referred to as dome pyroclasts). In reality, there is an overlap in the porosity range of the two populations. The juvenile pyroclasts analyzed are mostly lapilli in the grain size fraction 16–32 mm, with a few larger lapilli of the fraction 32–64 mm (Table 1).

Pumice pyroclasts are beige-gray in color and range from highly rounded to highly angular in shape (Fig. 2a, c, d) which may reflect (i) a mixed mode of tephra emplacement between PDC and fallout, with more abrasion and rounding for the PDC pyroclasts (Colombier et al. 2017a) or (ii) different degree of rounding due to variable porosities in this population. Rare breadcrust textures have been observed in a few, dense pumice lapilli and bombs. On the other hand, dome pyroclasts are gray to dark-gray and are essentially angular, with only a few sub-rounded particles (Fig. 2b). Some of these pyroclasts show breadcrust textures (Fig. 2e) and banded pyroclasts are ubiquitous in this population (Fig. 2f).

Pumice pyroclasts contain near-spherical to deformed vesicles (Fig. 3a–d). The degree of deformation of the vesicles seems to intensify with decreasing porosity and increasing crystallinity (Fig. 3a–d).

The range of textures in the dome pyroclasts population is highly variable between pyroclasts of similar porosity. We identify three main populations of dome pyroclasts: (i) a Type 1 consisting of dome pyroclasts with small isolated vesicles and larger coalesced vesicles organized in clusters within interstitial glassy areas between microlites (crystallinity is lower than in Type 2 pyroclasts; Fig. 3e–g); (ii) a Type 2 population with pyroclasts characterized by diktytaxitic textures with a high number density of small interconnected vesicles in a nearly holocrystalline matrix, and by the presence of cristobalite in interconnected vesicle clusters (Fig. 3h–j); (iii) a Type 3 population including brecciated dome pyroclasts with banded and sheared textural layers alternating with more brecciated domains consisting of granular patches with variable degree of sintering (Fig. 3k, l). The banded areas contain large phenocrysts of feldspar, kaersutite, biotite and occasionally, cristobalite, and ash particles and the grain size is highly variable.

Networks of pyroclast-wide cracks are present in all dome pyroclasts but are more developed in the Type 2 and 3 populations. We also observed locally interconnected vesicle chains in pumice and dome pyroclasts (Fig. 4a, b). These different textural lithologies are present in all the deposits associated with Vulcanian episodes of the Kilian eruption (Colombier et al. 2017a).

Finally, the in situ dome rock sample coming from the external part of dome remnants cropping out in Kilian crater shows textures similar to that of the Type 2 dome pyroclasts from the deposits. Similarities include the diktytaxitic texture with a holocrystalline matrix and absence of glass and the presence of cristobalite in the interconnected vesicles clusters highlighted by chemical mapping (Fig. 4f, g).

Chemical analysis and crystallinity

All the pyroclasts are trachytic in bulk rock composition (Fig. 5; Table SM1). No bulk rock oxide concentrations correlate

Table 1 Sample name, type, characteristics and methods applied for the different pyroclasts analyzed in this study. Superscript [a] refers to data taken from Colombier et al. (2017a)

Sample	Sample type		Grain size fraction (mm)	Porosity[a]	Permeability[a]	Crystallinity SEM[a] (vol %)	Crystallinity XRD (vol %)	Presence of cristobalite	EPMA glass	XRF	Textural observations
K2_1	Pumice; pyroclast		16–32	0.6	-	-	45.4	-	-	Yes	-
K1_s_1			16–32	0.6	-	-	54.4	-	-	-	-
U1-t-77			16–32	0.75	-	11	40.4	-	Yes	Yes	Yes
U1_b_28			16–32	0.77	-	8.5	-	-	Yes	-	Yes
K1_t_1			16–32	0.73	7.7×10^{-13}	13	-	-	Yes	-	Yes
U1_b_63			32–64	0.57	2.5×10^{-12}	17.5	49.9	-	Yes	Yes	Yes
K1_t_63			16–32	0.54	1.5×10^{-13}	25.5	46.7	-	-	-	Yes
U2_b_29*			32–64	0.6	2.7×10^{-12}	23.9	51.6	-	-	Yes	Yes
U1_t_3			32–64	0.44	6.2×10^{-13}	-	65.2	-	-	Yes	-
K2 Mul 2			16–32	0.48	-	-	53.2	-	-	-	-
U1_b_71			16–32	0.5	1.3×10^{-12}	23	-	-	Yes	-	Yes
K1_b_61	Dome rocks; pyroclast	Type 1	16–32	0.18	-	27	66.7	-	Yes	-	Yes
K1_s_2			16–32	0.27	-	-	69.1	Yes	Yes	Yes	-
K2 Mul 3			16–32	0.39	3×10^{-12}	-	-	-	-	-	Yes
K2 Mul 4			16–32	0.39	1.4×10^{-12}	-	-	-	-	-	Yes
U1_b_97			16–32	0.14	-	38	-	-	Yes	-	Yes
PB11-1803-2b1			-	-	-	-	-	-	-	-	-
K2 Mul 5		Type 2	16–32	0.21	6.6×10^{-13}	-	83.9	Yes	-	Yes	Yes
U1_t_6			32–64	0.23	1.6×10^{-12}	-	89.1	Yes	-	Yes	Yes
K1_t_64			16–32	0.13	2.7×10^{-15}	55	-	Yes	-	-	Yes
U1_b_96			16–32	0.19	-	47	-	Yes	-	-	Yes
U1-t-2			-	0.2	3.9×10^{-16}	-	-	Yes	-	-	Yes
K1_b_4			16–32	0.21	-	-	-	Yes	-	-	Yes
K1-s-3			-					Yes			Yes
K2_s_2		Type 3	16–32	0.27	-	-	-	-	-	-	Yes
U1_t_4			16–32	0.27	1.4×10^{-13}	-	59.51	-	Yes	Yes	Yes
PB11-1803-2a			-	-	-	-	-	Yes	Yes	-	Yes
PB11-1803-2c			-	-	-	-	-	Yes	Yes	-	Yes
K2_s_3			16–32	0.19	-	-	-	-	-	-	Yes
U1_b_81			-	-	-	-	-	-	-	-	Yes
BPK-1	In situ Type 2 dome rock; sampled at the exterior of the dome		-	-	-	-	-	Yes	-	-	Yes; chemical mapping

* clast from Sub-Plinian activity

[a] Data from Colombier et al. 2017

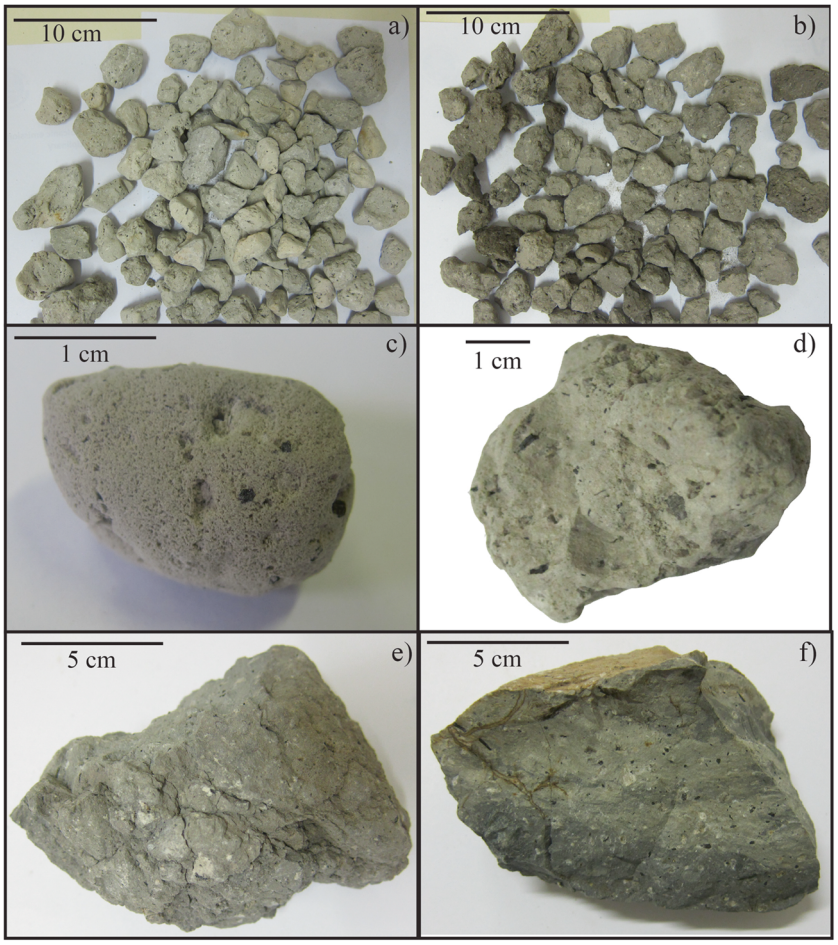

Fig. 2 The different types of pyroclasts erupted during Vulcanian activity at Kilian Volcano. **a** Pumices in the 32–64-mm grain size fraction with beige-gray color and showing variations in density and degree of rounding. (b) Dense, gray to dark-gray dome pyroclasts in the 32–64 mm fraction showing a higher apparent density than pumice pyroclasts and mostly angular shapes with only a few sub-rounded pyroclasts. **c** Highly vesicular, well rounded pumice pyroclast. **d** Denser pumice pyroclast with less rounded shape. **e** Dense dome pyroclast with breadcrusted surface. **f** Type 3 dome pyroclast with banded texture

with pyroclast type except for SiO_2, which is slightly higher in the Type 2 dome pyroclasts than in the Type 1 and Type 3 dome pyroclasts and pumice pyroclasts due to the presence of cristobalite (Table SM1). Glass compositions evolve from dominantly trachytic in the pumice pyroclasts to dominantly rhyolitic in the dome pyroclasts (Fig. 5; Table SM1).

The principal phenocrysts identified by microprobe are oligoclase and anorthoclase with minor amounts of kaersutite, magnetite, ilmenite, apatite, cristobalite, and zircon. The samples analyzed here lack phenocrysts of clinopyroxene although previous studies noted the presence of rare clinopyroxene in Kilian Tephra (Juvigné et al. 1992; Martel et al. 2013). The microlites are essentially oligoclase to anorthoclase feldspars (Fig. 5) and Fe-Ti oxides. Oxide nanolites (< 1 μm) are also abundant in Type 1 and 2 dome pyroclasts and frequently decorate feldspar microlites (Fig. 4d, e; Colombier et al. 2017a). We note that rare submicron nano-crystals were also occasionally observed in pumice pyroclasts. The number density of Fe-Ti oxide nanolites and microlites is considerably higher in dome pyroclasts than in pumice pyroclasts, as reported for other Vulcanian eruptions (Mujin and Nakamura 2014).

XRD analysis yields the identity and quantity of crystalline phases in the pyroclasts (Fig. 6a; Table 2). Phase proportions in wt% were converted to volume fractions using the known densities of the glass and crystalline phases. Although Fe-Ti oxide microlites and nanolites are ubiquitous in these samples and have a high number density (Colombier et al. 2017a), they were not detected by XRD implying that Fe-Ti oxides represent each less than 2 wt% (XRD detection limit) in all pyroclasts. The crystallinity estimated from XRD ranges from 50 to 94 vol% (Table 2). The most abundant phases are oligoclase and anorthoclase (50–87 vol%). Kaersutite is found only in one Type 1 dome pyroclast (2.2 vol%) and cristobalite appears mostly in the Type 2 dome pyroclasts (~ 6.5 vol%), and in smaller amount in one Type 1 dome pyroclast only (~ 4 vol%; Table 2).

Porosity distributions (Colombier et al. 2017a) are bimodal, with pumice and dome pyroclast populations centered around ~ 60% and 25% porosities respectively (Fig. 6b). The crystallinity of pyroclasts clearly increases with decreasing porosity (or increasing density) (Fig. 6a). The dome pyroclasts show crystallinities between 68.4 and 93.5 vol% whereas the pumice pyroclasts contain 49.9–66.7 vol% crystals. The crystallinities obtained by XRD and via 2D image

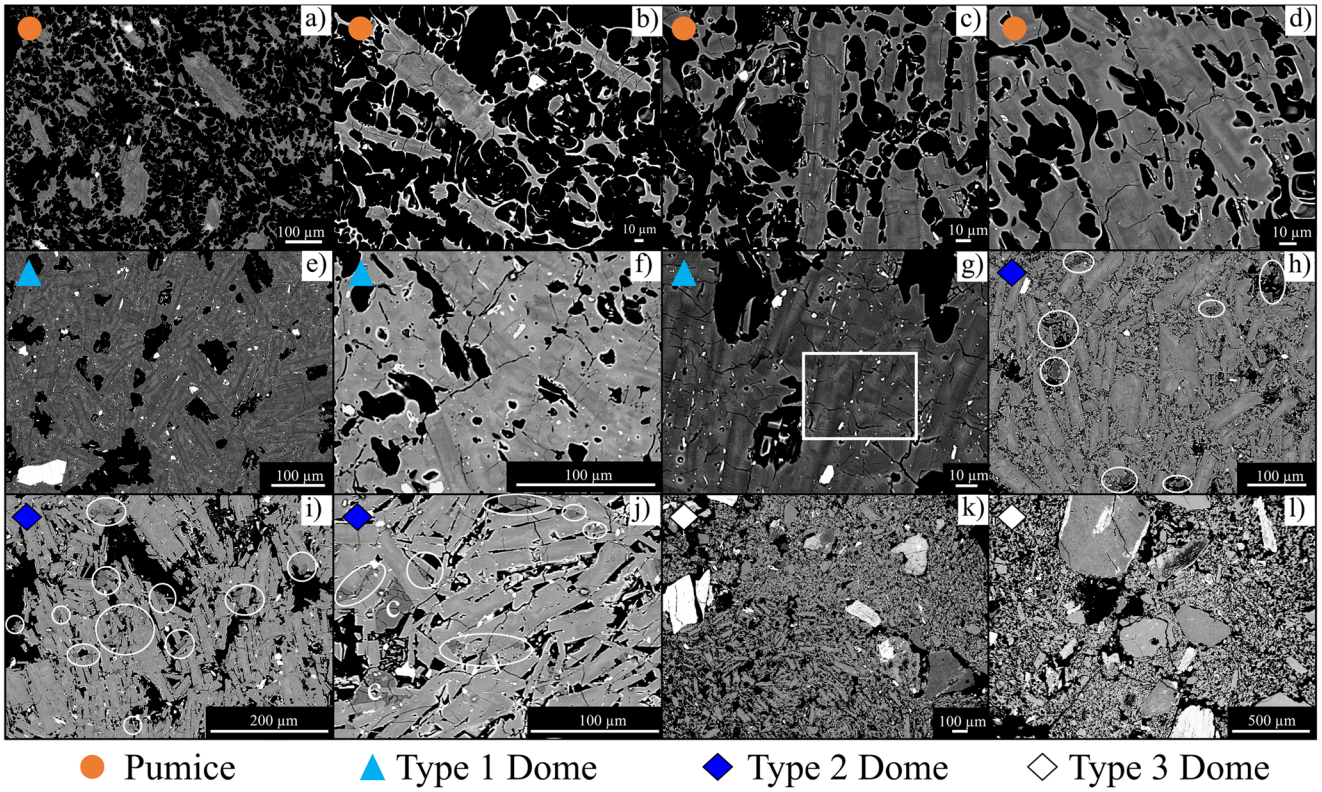

Fig. 3 Textural classification of the Kilian pyroclasts. The four main types of pyroclasts are shown: pumice pyroclasts (**a**–**d**), Type 1 (**e**–**g**), Type 2 (**h**–**j**), and Type 3 (**k**, **l**) dome pyroclasts. **a**, **b** Highly vesicular pumice pyroclast U1-t-77 with sub-spherical vesicles. **c**, **d** Pumice pyroclasts U1-b-63 and U1-b-71 with lower porosity, higher crystallinity, and degree of vesicle deformation. **e**–**g** Type 1 dome pyroclasts U1-b-97 and K1-s-2 with low porosity, high crystallinity, and interstitial glass between feldspar microlites. **h**–**j** Type 2 dome pyroclasts U1-b-96, K1-s-3, and U1-t-6 with diktytaxitic texture and presence of cristobalite in the interconnected vesicle clusters. Ellipsoids mark areas where cristobalite is observed. **k**, **l** Type 3 dome pyroclast PB11-1803-2c with granular material in between bands of variable porosity

analysis (Colombier et al. 2017a) show the same trend of increasing crystallinity with porosity, but values of crystallinity measured using image analysis are systematically 30–40 vol% lower than those obtained with XRD (Fig. 6a). We note that crystallinity is expressed on a vesicle-free basis for both techniques. XRD analyses carry an inherent error for multi-component rock samples. Based on the different crystal structures and symmetries of the involved phases, they have a different X-ray scattering power, possibly leading to an underestimation of bad diffractor phases with a low scattering power (e.g., feldspars and/or amphiboles) (Dunn et al. 2010). However, in the trachytes studied here, the most abundant crystalline phases are feldspars based on textural and chemical observations, with only minor amounts of other minerals. A calibration of the XRD technique for crystallinity quantification based on a mixture of varying amounts of feldspar and glass showed that the error is less than 5 vol% with this method (Fig. SM3 in the Supplementary Material), which implies that the discrepancy between XRD and image analysis mostly arises from issues with the latter technique. Limits to contrast in the scanning electron microscope images and the fact that microlites below a certain size cannot be resolved and quantified may be responsible for this apparent discrepancy in crystallinity. Rowe et al. (2012) have discussed that two-dimensional imaging techniques are insufficient for characterizing crystallinity in samples where the groundmass does not contain an easily identifiable glassy component, which is the case here for Kilian samples. D'Oriano et al. (2005) have pointed out that feldspar composition for trachytic-phonolitic melts is close to that of the residual liquid and that subsequent low grey scale contrast of feldspars and matrix glass on BSE images constitute an obstacle for detailed textural analysis. This discrepancy between XRD and image analysis is likely more significant in highly crystal-rich samples such as Kilian trachytes. Devitrification and the presence of high quantities of small crystals not quantified during image treatment may be an additional cause of discrepancy between crystallinities measured by XRD and image analysis (Rowe et al. 2012; de Andrade et al. 2017). Regardless of the method, data obtained by the two techniques show similar features, with Type 1 dome pyroclasts being less crystalline than Type 2 dome pyroclasts (Fig. 6a; Tables 1 and 2). Interestingly, the crystallinity increases with decreasing porosity in the pumice population, and the least vesicular pumice has crystallinities

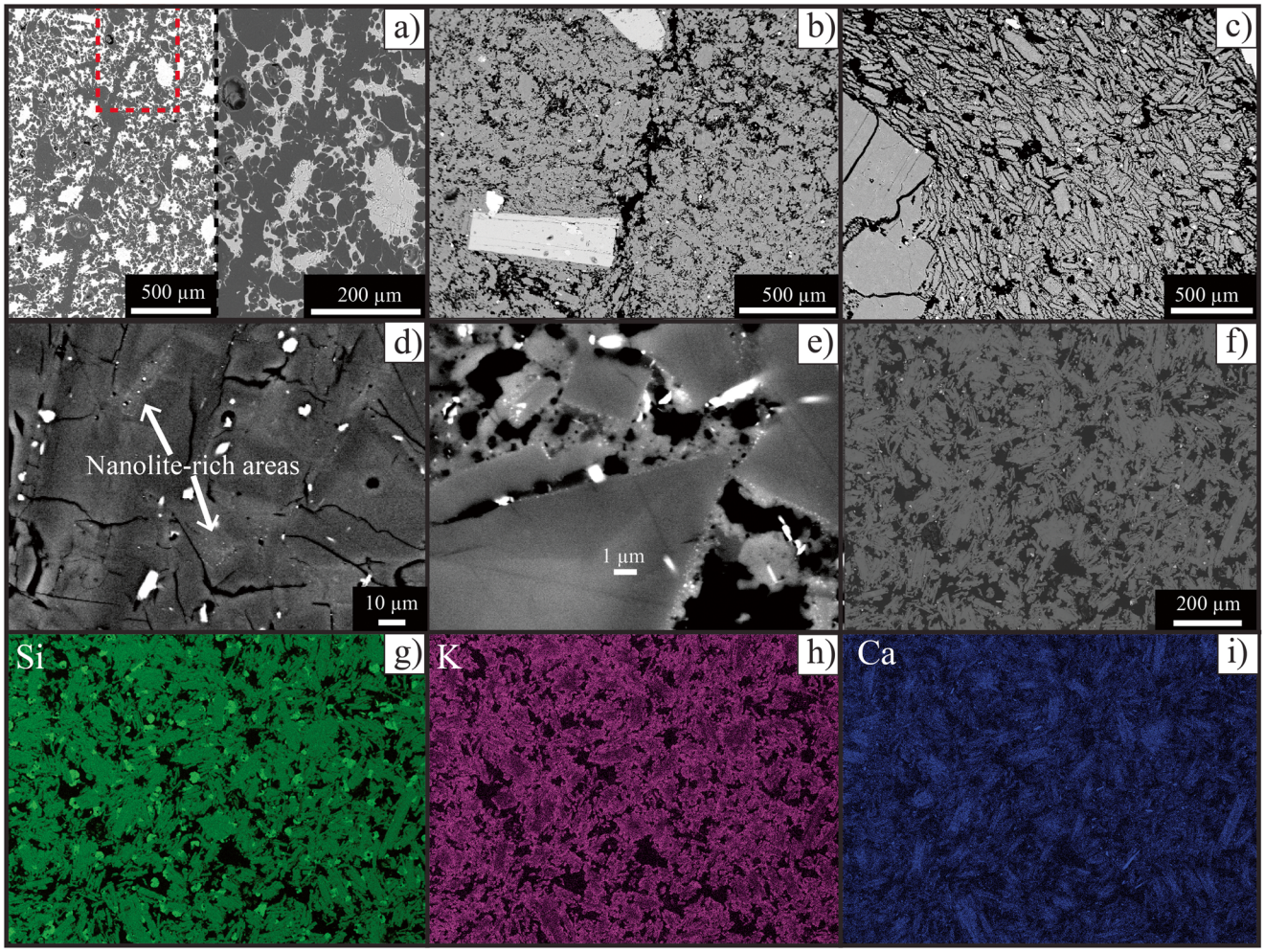

Fig. 4 Specific textural features observed in the trachytes. Images **a** to **f** are back-scattered electron images, and images **g** to **i** are compositional maps. **a** Pumice pyroclast K1_t_1 with fracture-like chain of coalesced vesicles in the right panel. **b** Fracture-like chain of coalesced vesicles in the Type 1 dome pyroclast K2Mul3. **c** Type 1 dome pyroclast PB11_1803_2b1 showing trachytic texture with aligned microlites. **d** Oxide nanolites in the interstitial glass between feldspar microlites in Type 1 dome pyroclast U1-b-97. Due to limitations in image magnification, nanolites appear as bright dots only 1 or 2 pixels in width in this pyroclast and arrows are to guide the eye towards regions with high nanolite concentration. Note that the nanolites should not be confused with microlites (larger than 1 µm). **e** Oxide nanolites in the interstitial glass between feldspar microlites in the Type 2 dome pyroclast U1-b-96. Nanolites are commonly arranged as rims around the feldspar microlites in this sample. **f**–**i** Scanning electron microscope images and chemical map for Si, K, and Ca in the in situ dome rock BPK-1 sampled at the exterior of the dome remnants of Kilian crater. This dome rock has a Type 2 characteristic diktytaxitic texture with the presence of cristobalite evidenced in the chemical map of Si (g)

approaching some of the Type 1 dome pyroclasts (Fig. 6a; Tables 1 and 2). Only one Type 3 banded-pyroclast was measured and showed the lowest crystallinity in the dome population (68.4 vol%).

Glass compositions

The glass compositions of pumice and Type 1 dome clasts form a nearly continuous spectrum of increasing SiO_2 and decreasing Al_2O_3 and alkali content, likely associated with extensive feldspar microlite crystallization (Fig. 7). More generally, elements that are compatible in anorthoclase (Al_2O_3, Na_2O, CaO) show trends consistent with extensive feldspar crystallization. By contrast, MgO is incompatible in anorthoclase, yet also decreases with increasing SiO_2. We attribute this decrease to crystallization of kaersutite containing ~ 10 wt% MgO on average. Cl is also incompatible in most crystallizing phases (kaersutite contains only up to 0.15 wt% in these rocks) and should increase in the melt during crystallization. However, Cl slightly decreases with increasing SiO_2 in the interstitial glass between pumice and dome pyroclast, suggesting possible loss to degassing (Fig. 7). The composition of the most vesicular pumice pyroclasts matches closely the composition of melt inclusions trapped in amphiboles and plagioclase phenocrysts (Martel et al. 2013), suggesting little crystallization occurred between the time when inclusions were trapped and the least crystal-rich pumice pyroclasts were erupted. In addition, SiO_2, TiO_2, and

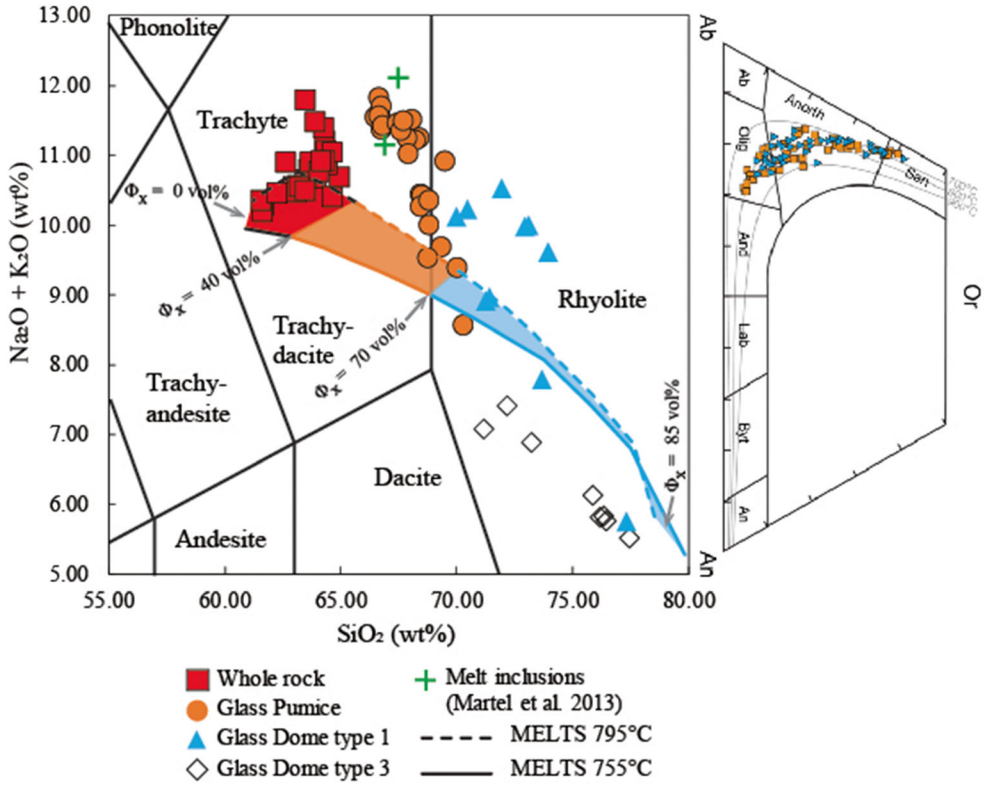

Fig. 5 Total alkali versus SiO_2 diagram showing whole rock compositions of the pyroclasts (red squares) and glass compositions of pumice pyroclasts and Type 1 and 3 dome pyroclasts. This diagram was modified after Le Bas et al. 1986. Glass is absent or rare in the Type 2 dome pyroclasts explaining the lack of data for this pyroclast population. The solid and dashed curves correspond to the evolution of melt composition during crystallization modelled using Rhyolite-MELTS at 755 and 795 °C, respectively. The modelled trend was separated according to magma crystallinity (Φ_x): 0–40 vol% (red shaded area); 40–70 vol% (typical of pumice population; orange shaded area), and 70–85 vol% (typical of dome pyroclasts; blue shaded area). The inset on the right represents a feldspar ternary made using the data along with isotherms calculated using SOLVCALC (Wen and Nekvasil 1994). Ab: Albite; Olig: oligoclase; And: Andesine; Lab: Labradorite; Byt: Bytownite; An: Anorthite; San: Sanidine. Error bars are smaller than symbols

Table 2 Crystallinities and glass content obtained by XRD. All other phases represent less than 2 vol % of the samples and were not considered for the analysis

Sample	Sample type	Porosity	Crystallinity	Proportion of phases (vol %)					
				Anorthoclase	Oligoclase	Kaersutite	Cristobalite	Glass	χ^2
K1_t_63	Pumice	0.54	53.2	26.8	26.3	-	-	46.8	1.21
U2_b_29	Pumice	0.6	65.5	36.3	29.3	-	-	34.5	1.27
U1_b_63	Pumice	0.57	61.5	23.6	37.9	-	-	38.5	1.32
U1_t_3	Pumice	0.44	66.7	37.1	29.6	-	-	33.3	1.1
U1_t_77	Pumice	0.75	49.9	26.0	24.0	-	-	50.1	1.04
K1_s_1	Pumice	0.6	62.9	27.5	35.4	-	-	37.1	1.2
K2 Mul 2	Pumice	0.48	58.1	25.3	32.8	-	-	41.9	1.31
K2_1	Pumice	0.6	51.8	14.9	36.9	-	-	48.2	1.17
K1_b_61	Dome Type 1	0.18	74.0	35.3	36.4	2.2	-	26.0	1.4
K1_s_2	Dome Type 1	0.27	76.7	32.8	40.0	-	3.9	23.3	2.21
K2 Mul 5	Dome Type 2	0.21	93.5	67.9	19.1	-	6.5	6.5	1.5
U1_t_6	Dome Type 2	0.23	82.9	24.7	51.9	-	6.3	17.1	1.92
U1_t_4	Dome Type 3	0.18	68.4	31.5	36.9	-	-	31.6	3.54

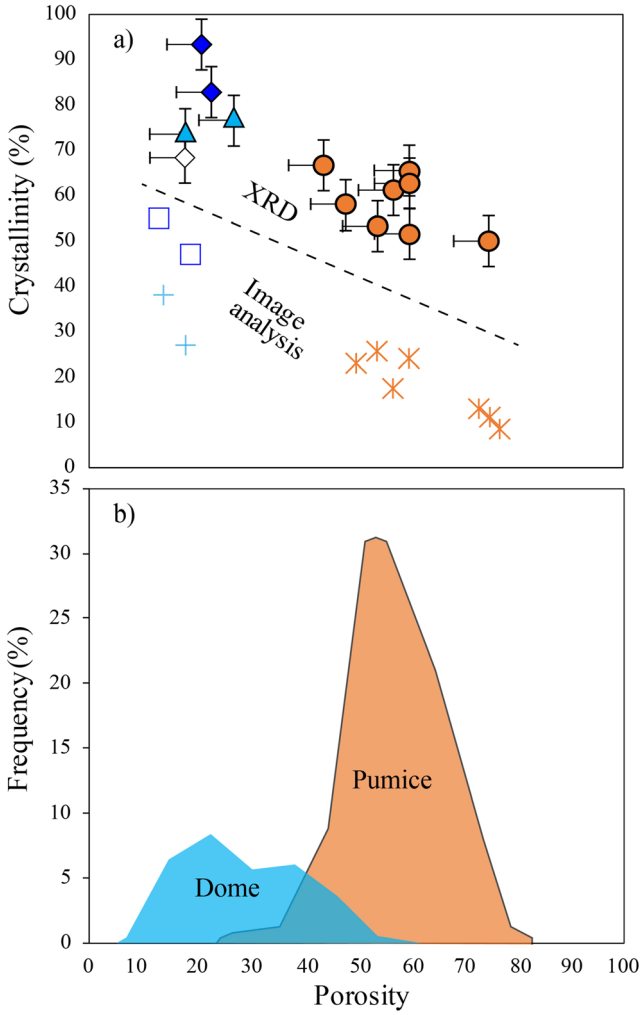

Fig. 6 **a** Crystallinity (vesicle-free) vs. porosity in the pyroclasts. Orange stars, blue crosses, and blue open squares represent data obtained by 2D image analysis for pumice pyroclasts, Type 1 and Type 2 dome pyroclasts, respectively (Colombier et al. 2017a). Orange circles, blue triangles, dark blue diamonds, and open diamonds represent XRD data from this study for pumice pyroclasts, Type 1, Type 2, and Type 3 dome pyroclasts, respectively. **b** Porosity histogram showing the dome and pumice populations overlapping

Fe_2O_3 are higher in the dome glass (Types 1 and 3) compared to the pumice glass, while MgO, CaO, Na_2O, K_2O, Al_2O_3, and Cl are higher in the pumice glass (Fig. 8). F content in the glass was below the detection limit (500 ppm). The Type 3 dome pyroclasts (banded and brecciated pyroclasts) have a similar range in glass SiO_2 compared to Type 1 dome pyroclasts, but with lower average values for alkalis, TiO_2, Fe_2O_3, and MnO and higher values of MgO, Al_2O_3, CaO, and P_2O_5 (Figs. 5, 7, and 8; Table SM1 in the Supplementary Material). This evolution of glass composition from vesicular pumice to denser dome pyroclasts likely reflects the predominant crystallization of feldspars together with minor amounts of magnetite microlites.

Chemical mapping revealed a zonation in the feldspar microlites in the dome pyroclasts, with large microlites showing more Ca-rich and K-poor cores than rims and smaller microlites (Fig. 4). Therefore, the large variations in K_2O and CaO observed for feldspar composition in Fig. 7 likely reflect an evolution in time toward higher and lower values of K_2O and CaO, respectively, during feldspar crystallization. This observation agrees with the fact that data for feldspar phenocrysts formed early in the crystallization process plot towards the CaO-rich and K_2O-poor endmember of the feldspar population (Fig. 7).

Viscosity model

The thermal analysis yielded a glass transition temperature T_g ~ 689 °C (Fig. 9). We then estimated the dry and hydrous melt viscosity and magmatic water content of the trachytic magma by combining the viscosity models of Gottsmann et al. (2002) and Giordano et al. (2004). A detailed description of the procedure and error estimation is given in the Supplementary Material. Output of the model yielded a water content of 0.04 wt% and a viscosity of $10^{11.07}$ Pa.s at T_g in the pumice population. The viscosity with this model assuming a similar water content at eruptive temperature of 775 °C (Martel et al. 2013) for the pumice population yielded ~ $10^{9.38}$ Pa.s. We emphasize that these viscosity estimates represent the values at the time of quenching of the pumice pyroclasts, and viscosity may have been significantly lower during fragmentation if the water content was higher. At pre-eruptive storage conditions of 300–400 MPa, ~ 8 wt% H_2O, and T = 775 °C (Martel et al. 2013), the model yields a melt viscosity $10^{1.71}$ Pa.s.

The low modelled magmatic water content in the glass of the pumice pyroclasts at the time of quenching compares nicely with the results of the thermogravimetric analysis (Fig. 9). This analysis shows mass loss only below T_g, suggesting the presence of some meteoric water but no magmatic water in pumice and dome pyroclasts (Giachetti et al. 2015). We note that Cl was likely stabilized in the melt phase during this thermal treatment due to the high iron content preventing volatilization and Cl escape (Dingwell and Hess 1998). Next, we used the Giordano et al. (2008) model to calculate the melt viscosity of the Type 1 dome pyroclasts with a rhyolitic glass composition and assuming a water content of 0.02 (lowest solubility for rhyolitic composition). This yielded a viscosity of ~ $10^{11.69}$ Pa.s at 775 °C.

Discussion

Origin of the different types of pyroclasts

We hereafter combine information from textural and chemical analysis with viscosity estimates to shed light on the origin of the different types of pyroclasts and on conduit stratigraphy prior to Vulcanian episodes at Kilian Volcano.

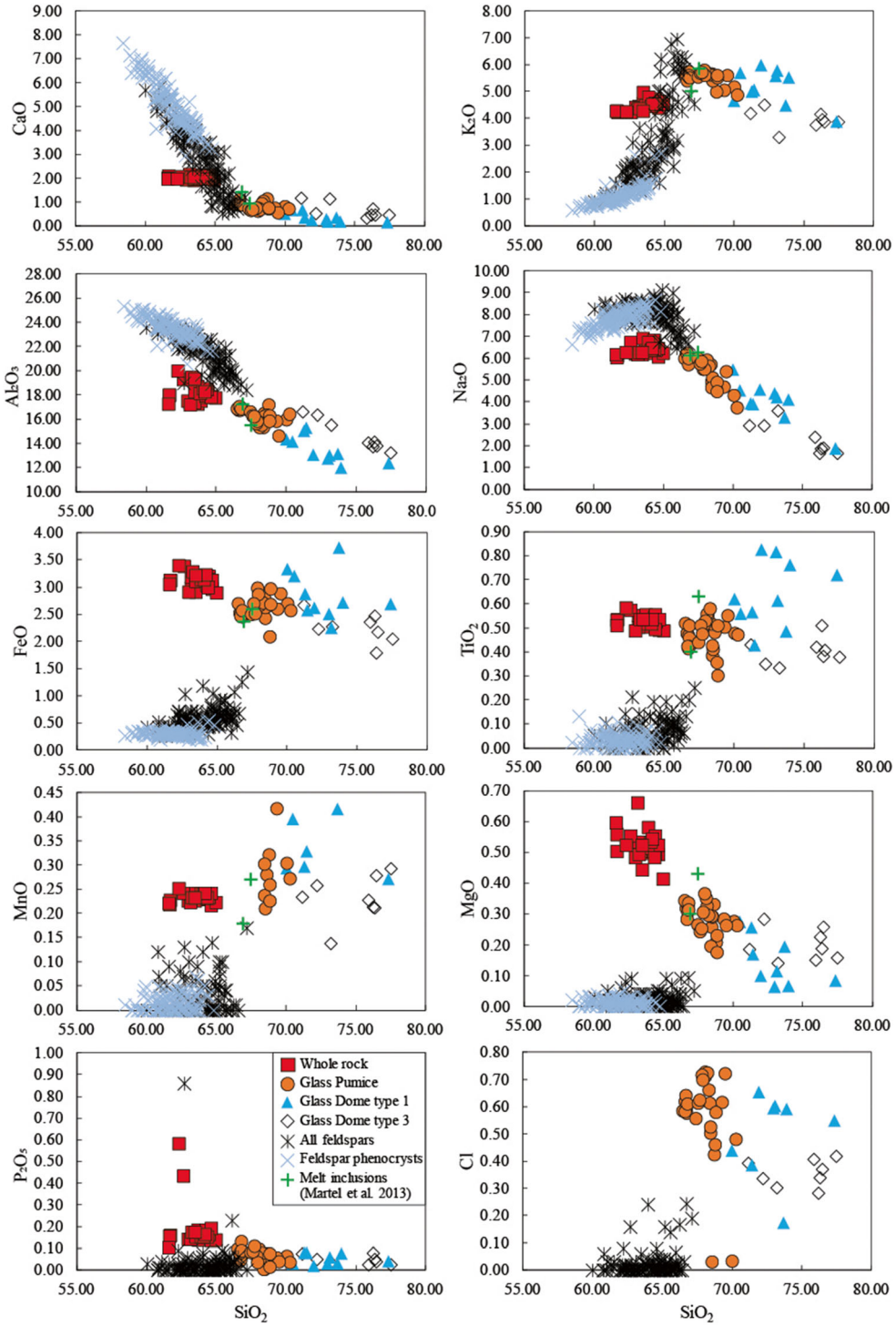

Fig. 7 Compositions of whole rocks, interstitial glasses, melt inclusions, and crystals. The interstitial glass compositions are for pumices, Type 1, and Type 3 dome pyroclasts. Glass is absent or rare in the Type 2 dome pyroclasts. Error bars are smaller than symbols

Pumice population

Glasses within the most vesicular pumice pyroclasts are similar in composition to melt inclusions measured in feldspar and amphibole phenocrysts by Martel et al. (2013). This similarity suggests that microlites did not significantly modify the melt composition in the pumice population after phenocryst formation.

Scanning electron microscope observations and XRD analysis indicate that crystallinity increases with decreasing porosity of the pumice pyroclasts. Furthermore, the crystallinity in the least vesicular pumice pyroclasts approaches values measured in some of the Type 1 dome pyroclasts (Fig. 6a). These pumice pyroclasts were therefore likely emplaced in an intermediate region below the

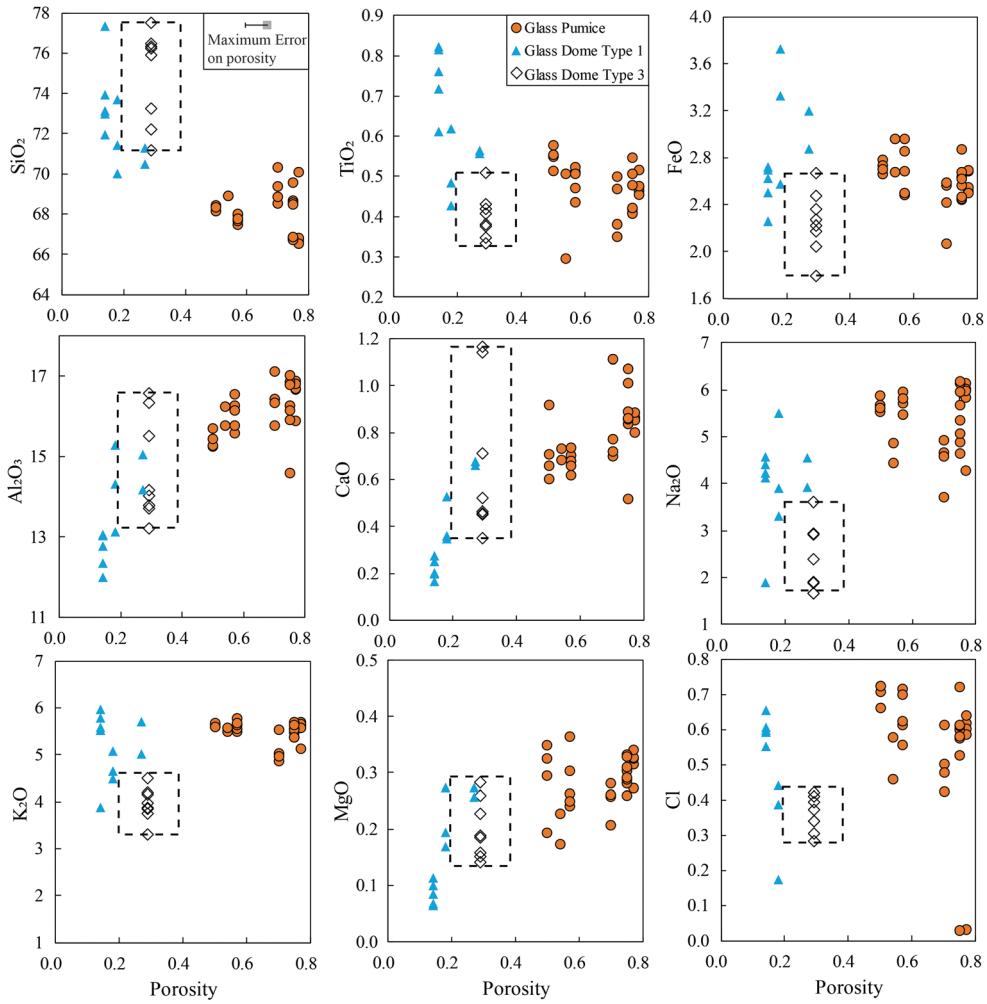

Fig. 8 Evolution of interstitial glass composition with whole pyroclast porosity. Orange circles: pumice glass. The dashed boxes show the range of porosities observed in the heterogenous Type 3 dome pyroclasts

dome, which experienced greater extents of decompression, cooling, degassing, and therefore more crystallization than deeper in the conduit. Alternatively, pumice pyroclasts with higher microlite content may originate from the conduit margins where (i) lower temperatures promote crystallization or (ii) preferential, strain-induced degassing (Shea et al. 2014) may have accelerated degassing-induced crystallization. These transitional zones might explain the overlap in crystallinity and porosity between the pumice and dome populations (Fig. 6).

High porosity pumice pyroclasts likely originate from deeper and more central zones of the conduit and experienced significant syn- and post-fragmentation vesiculation and possibly outgassing (Giachetti et al. 2010; Giachetti et al. 2015). This scenario would be consistent with the low magmatic water content modelled and measured in the pumice pyroclasts. Evidence for post-fragmentation vesiculation is also recorded by the presence of bread-crust textures at the surface of bombs and lapilli (Colombier et al. 2017a).

Type 1 dome pyroclasts

These dome pyroclasts are less crystalline than those of Type 2 but are more crystalline than most of the pumice and Type 3 pyroclasts. The melt composition during magma ascent was initially similar to that of pumice and melt inclusions and subsequently evolved by crystallization of mostly feldspar and minor amounts of kaersutite and magnetite. Measured glass compositions show more heterogenous and depleted Cl contents compared to the pumice population. Depleted and heterogenous Cl contents in volcanic rocks have been reported elsewhere and attributed to (i) leaching or devolatilization of Cl by escaping steam with subsequent degassing to the surface (e.g., Soufrière Hills volcano; Harford et al. 2003; Horwell et al. 2013; Schipper et al. 2019), (ii) outgassing (Yoshimura et al. 2019; Schipper et al. 2019), (iii) devitrification in rhyolitic melts (Schipper et al. 2019), or (iv) groundmass crystallization in a slowly cooling magma (Signorelli and Carroll 2002). The latter process can be ruled out as groundmass crystallization of microlites with low Cl content would have

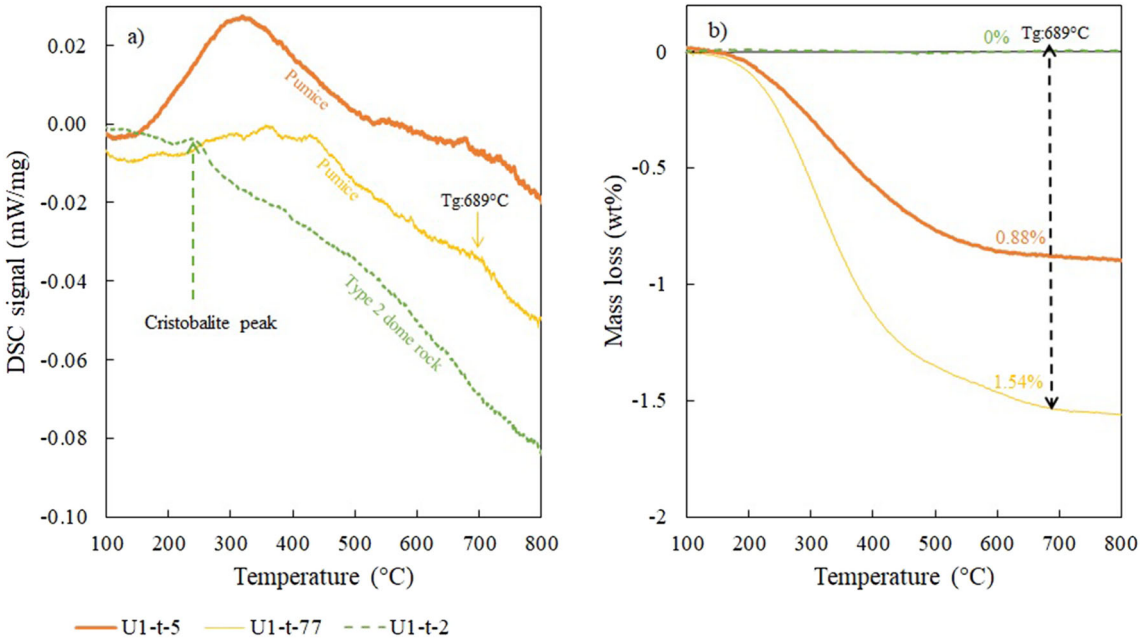

Fig. 9 Results from the simultaneous thermal analysis showing the quantification of the glass transition temperature using differential scanning calorimetry (**a**) and the mass loss related to meteoritic water content using thermogravimetric analysis (**b**). No significant water loss is observed after T_g is crossed, consistent with the results of the viscosity model indicating low magmatic water content. The raw data are presented without baseline correction due to the weak signal during analysis

the inverse effect of increasing the Cl content from pumice to dome pyroclasts. We thus propose that permeable gas and fluid transport are likely responsible for the heterogeneous and depleted Cl concentrations in the dome pyroclasts at Kilian. We note that a low Cl content was measured locally in two pumice pyroclasts, indicating that a similar process may also have occurred to a lesser extent and in more localized areas in the pumice population.

The presence of networks of large interconnected vesicle clusters and the high permeability (~ 10^{-12} m^2; Table 1) of Type 1 dome pyroclasts indicates that permeable gas escape likely occurred in this population (possibly aided by formation of cracks). Additional permeability measurements would be required to better explore differences between the four pyroclast populations. Cristobalite is generally rare in Type 1 samples but was observed in one pyroclast, with lower concentrations than those found in the Type 2 pyroclasts. The low cristobalite abundance relative to Type 2 pyroclasts in turn suggests more limited or later occurrence of outgassing and fluid transport. A population of small isolated vesicles coexists with the large vesicle clusters, previously attributed to a late stage event of syn-eruptive bubble nucleation and growth event (Colombier et al. 2017a). This late stage of bubble nucleation may have proceeded heterogeneously on feldspar and Fe-Ti microlites (Shea 2017; Pleše et al. 2018). The low connectivity and size of these small bubbles mean that this second vesiculation event likely had a small influence on permeability and outgassing compared with macropores.

Type 1 pyroclasts can be considered as a gradual transition between pumice pyroclasts and Type 2 rocks in terms of textures, composition, crystallinity, and the presence and amount of oxide nanolites and cristobalite (Figs. 3, 4, and 6; Table 2). As discussed above, pumice pyroclasts are inferred to represent hot vesicular magma beneath the lava dome. We argue in the next section that the Type 2 pyroclasts likely arise from the upper part of the dome (talus and carapace). We therefore propose that the Type 1 population corresponds to a transitional region in the interior of the dome above the underlying hot and less viscous magma and beneath the diktytaxitic carapace.

Type 2 dome pyroclasts

These pyroclasts display diktytaxitic textures, and are more crystal-rich than the Type 1 pyroclasts at a similar porosity with scarce glassy areas only recognized through XRD analyses (Fig. 6). The presence of this texture suggests either (i) more extensive crystallization, (ii) gas-filter pressing that may remove the highly viscous melt from these parts of the dome or (iii) dissolution of the glass through intense leaching.

Cristobalite microlites are present within scanning electron microscope and microprobe images in all Type 2 pyroclasts (Fig. 3; Tables 1 and 2). Cristobalite is almost systematically located in interconnected macro-pores that resemble the vesicle clusters observed in the Type 1 dome pyroclasts but with more irregular shapes due to higher crystallinities and smaller size indicative of more advanced pore collapse (Fig. 3). Thus,

cristobalite likely crystallized in the connected porous network of these dome pyroclasts. Cristobalite is frequently found in dome rocks with diktytaxitic textures from other lava domes and lavas such as at Lewotolo volcano, Soufrière Hills volcano in Montserrat, Volcán de Colima, Cordón Caulle, Merapi or Mount Taranaki (e.g., de Hoog et al. 2005; Williamson et al. 2010; Lavallée et al. 2012; Schipper et al. 2015; Kushnir et al. 2016; Preece et al. 2016; Zorn et al. 2018). Cristobalite has also been recognized in other Chaîne des Puys trachytic domes at Chopine and Puy de Dôme volcanoes (Boudon et al. 2015; Deniel et al. 2020). The presence of cristobalite is often taken as an evidence for prolonged residence time in the dome during outgassing (Kendrick et al. 2016) although cristobalite precipitation itself is believed to be a rapid process (typically in the order of few hours; Williamson et al. 2010; Damby et al. 2014). Cristobalite formation has been attributed to gas filter pressing (Kushnir et al. 2016), devitrification (e.g., Horwell et al. 2013; Schipper et al. 2015, 2017) and/or precipitation from silica-rich fluids percolating through the dome (Horwell et al. 2013; Boudon et al. 2015; Kendrick et al. 2016). In our case, the fact that cristobalite is always observed in the connected macro porosity suggests that it was formed by permeable transport of Si-rich fluids during outgassing and possibly hydrothermal activity at shallow levels.

The increase in bulk SiO_2 in Type 2 dome pyroclasts (Table SM1) suggests that silica was transported into this region of the dome from external sources outside the magmatic system, as proposed by Horwell et al. (2013), or from inner regions of the dome. The presence of cristobalite and diktytaxitic textures are characteristics of external regions of lava domes, and are typically found in the carapace or talus region (Boudon et al. 2015; Kushnir et al. 2016; Heap et al. 2018). We propose that the source of SiO_2 arises from leaching of Si-rich melt areas from the Type 1 interior region of the dome and subsequent transport to the external carapace or talus region. Leaching may proceed via corrosion through magmatic H_2O and/or acid solutions/vapors such as HF followed by scavenging of alkalis and Si present in the glass and crystalline phases, and subsequent entrainment in Si-rich fluids (Horwell et al. 2013; Schipper et al. 2015). This scenario can therefore be seen as intermediate between a "bulk transport" and a "local redistribution" of silica (Horwell et al. 2013; Schipper et al. 2015) in the case of Kilian with a process in which the vapor source comes from the dome itself (in agreement with local redistribution) but involves some transport and causes change in the bulk SiO_2 content (compatible with bulk transport).

This origin in the exterior of the dome is further suggested by the presence and high number density of Fe-Ti oxide nanolites in the Type 2 dome pyroclasts (e.g., Fig. 4e). Nanolite crystallization has been attributed to late stage crystallization in shallow regions, and cooling and oxidation as proposed by Mujin and Nakamura (2014) for Shinmoedake volcano (Japan). We note that these nanolites likely formed substrates for heterogeneous bubble nucleation, causing very high bubble number densities in some dome pyroclasts (Colombier et al. 2017a; Shea 2017; Cáceres et al. 2020).

Based on all these observations, we propose that these Type 2 dome pyroclasts originate from the exterior of the dome (carapace and talus), in which significant cooling, crystallization, and hydrothermal activity took place. This interpretation is further supported by the highly similar diktytaxitic texture and presence of cristobalite in connected vesicle clusters revealed by chemical mapping in the in situ dome rock corresponding to the external part of the dome remnants sampled at the rim of Kilian crater (Fig. 4f, g).

Type 3 dome pyroclasts

These pyroclasts display bands of distinct porosities enclosing variably sintered grains. These bands often consist of macrofractures containing microphenocrysts, phenocrysts, and ash particles. The sizes of the particles in the sintered zones differ strongly. Sintered pyroclasts are most likely relics of parts of the dome intersected by tuffisite veins, which may have acted both as fragmentation and outgassing pathways (e.g., Stasiuk et al. 1996; Tuffen et al. 2003; Kolzenburg et al. 2012; Castro et al. 2014; Kendrick et al. 2016; Saubin et al. 2016).

Although typical of crystal-poor rhyolitic magmas, evidence of sintering in tuffisite veins has also been recently recorded in crystal-rich magmas (Kendrick et al. 2016). Sintering involves welding of ash particles in a ductile manner, but solid-state sintering has also been shown experimentally as a plausible mechanism (Ryan et al. 2018). Tuffisite veins can be generated in new fractures or use pre-existing veins (Kendrick et al. 2016). Sintering reduces both porosity and permeability with time (Wadsworth et al. 2017; Heap et al. 2019). Variable degree of sintering due to different P-T-t conditions can accordingly lead to a broad range of values of porosities and permeabilities in the tuffisite pyroclasts. Hence, tuffisite veins can initially promote outgassing during fracturing and ash-jetting stage, yet also cause dome overpressurization during the ash accumulation and sintering stages.

Fractures hosting tuffisites generally form via multiple fragmentation events and gas- and ash-explosions, as observed at Colima volcano (Kendrick et al. 2016) and during Vulcanian activity at Chaitén volcano (Saubin et al. 2016). We noted the presence of tuffisite pyroclasts in all the deposits associated with Vulcanian phases. We can therefore propose that each Vulcanian episode during the Kilian eruption was preceded by repeated fragmentation events, possibly including gas- and ash-explosions.

The variable degrees of sintering in different pyroclasts may reflect sintering at different temperature conditions in

the different parts of the dome. Sintering in the colder carapace and talus regions likely occurred at lower temperature, therefore welding was less efficient, and tuffisite preserved a granular, brecciated aspect (Fig. 3k, l). On the other hand, the degree of welding was higher in the interior of the dome, causing the fractures to seal almost completely, leading to the banded textures.

The glass in the non-granular groundmass of Type 3 pyroclasts is similar to that of Type 1 dome pyroclasts, but with peculiar chemical signatures (e.g., Fig. 5, 7, and 8). This may be explained by a lower crystallinity of Type 3 pyroclasts, as suggested by the XRD data (Fig. 6).

Controls on eruptive style during trachytic Vulcanian eruptions

We discuss the processes promoting outgassing versus overpressure and the implications for effusive-explosive transitions at Kilian Volcano before comparing crystallization and outgassing processes in Kilian trachyte to other silicic magmas to unravel the peculiarities of trachytic Vulcanian eruptions.

Conduit stratigraphy during the dome-forming phases of Kilian Volcano and comparison with other volcanoes

The textural and chemical transition from pumice to Type 1 to Type 2 dome pyroclasts provides insights into the stratigraphy of the conduit prior to Vulcanian episodes. As we infer the replenishment of conduit prior to a Vulcanian eruption to occur in a single batch of magma ascent (Wright et al. 2007), we propose that the differences in crystallinity between the pyroclast types reflect differences in location in the conduit rather than residence time (as proposed by Couch et al. 2003). The high crystallinity of Type 2 dome pyroclasts can be explained by (i) decompression to shallower depths, (ii) greater cooling, and (iii) more extensive degassing leading to the formation of a highly viscous carapace. The parent magma of Type 1 "glassy" dome was emplaced underneath this carapace, with more limited decompression and likely absence of cooling causing less crystallization. Finally, the parental magma of the pumice pyroclasts resided deeper in the conduit at the time of Vulcanian excavation, with less decompression than in the Type 1 dome, causing lower crystallinities. The Type 3 magma was likely emplaced by granular sintering following gas and ash explosions and ensuing settling of the ash particles in the fractures. We propose a schematic representation of the dome growth at Kilian in Fig. 10.

We note that similar vertical pyroclast transition from pumice to glass-bearing dome and more crystal-rich dome was also observed for Soufrière Hills volcano (SHV) in Montserrat (Couch et al. 2003). Couch et al. (2003) specify that the glassy dome samples have crystallinities and compositions intermediate between the pumice and crystalline dome samples at SHV. They also show that cooling only plays a role in the outermost parts of the dome (carapace). This similarity in lithology is additional evidence that the 9.4 ka Kilian Vulcanian phases were analogous to Vulcanian activity at Soufrière Hills volcano in terms of conduit stratigraphy, as proposed by Colombier et al. (2017a).

The model of conduit proposed here with an outermost crystal-rich carapace at Kilian Volcano contrasts with other models of plug/dome forming eruptions that commonly infer lower crystallinity in the carapace due to faster quenching (Shea et al. 2017; Zorn et al. 2018). On the other hand, similarities with previous eruptive scenarios exist. Kushnir et al. (2016) and Heap et al. (2018), for instance, also attribute the diktytaxitic textures observed in the Type 2 pyroclasts to a low permeability cap in the carapace and talus regions.

Outgassing vs. pressurization in crystal-rich trachytic magmas

The products of the Kilian eruption suggest that outgassing was significant in the magma column prior to each Vulcanian phase. Outgassing was likely promoted by enhanced bubble coalescence in a crystal-rich magma (e.g., Oppenheimer et al. 2015; Lindoo et al. 2017; Colombier et al. 2020), brittle fracturing (Lamur et al. 2017), and by fracture-like and intergranular connected pore space in tuffisite veins (Type 3 dome pyroclasts; Heap et al. 2019). The dominant pathways of gas escape and fluid transport occur along interconnected vesicle clusters and tuffisite veins, and extensive precipitation of cristobalite appears to have been restricted to the exterior of the dome. We note that the usual development of shear fractures was rarely observed at the scale of the tephra, but likely had an important role on large-scale outgassing in the trachytic dome (Gaunt et al. 2014). Outgassing also occurred in the dome interior and the pumice parental magma prior to the eruption through connected vesicle networks, and occasionally led to the formation of cristobalite in the dome interior. The low magmatic water contents in the pumice pyroclasts also indicate important pre- or post-fragmentation degassing/outgassing in this population (Giachetti et al. 2015). Permeable gas escape in the pumice may occur through coalesced bubbles and bubble chains resembling fracture-like geometries described elsewhere in crystal-rich volcanic rocks and magma analogues (e.g., Oppenheimer et al. 2015; Parmigiani et al. 2016; Colombier et al. 2020; Heinrich et al. 2020).

Pressurization in the conduit prior to the Vulcanian episodes may be explained by a low magma permeability reducing gas escape and promoting the buildup of fragmentation, possibly triggering fragmentation. A low permeability may be caused by (i) late bubble coalescence and outgassing in the hot vesicular magma underneath the lava dome, (ii) bubble collapse and isolation of the porous network in the dome, (iii)

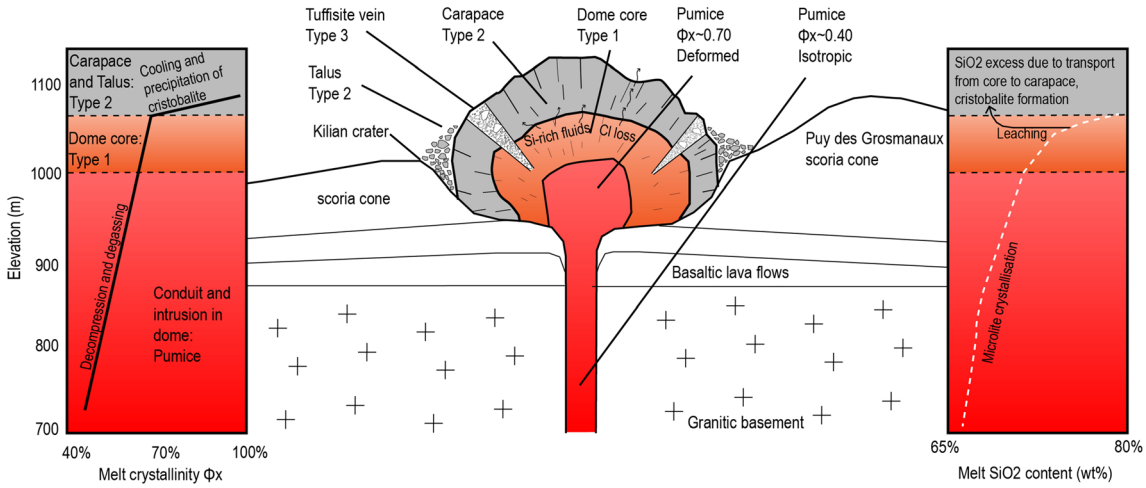

Fig. 10 Conceptual model showing the textural and chemical evolution as a function of conduit stratigraphy during effusive-explosive transitions at Kilian Volcano. The sketch illustrating dome emplacement is not to scale although the contours of the dome and pre-existing topography were inspired from geophysical studies in the area (Portal et al. 2016) and numerical models of endogenous dome growth (Harnett et al. 2018). The possible evolution of magma crystallinity and melt SiO_2 content based on the XRD and microprobe data are illustrated as a function of vertical position above the conduit. The color code was chosen to illustrate the relative temperature variations (grey: colder; orange: intermediate; red: hotter). Tuffisite veins are unrealistically wide for illustration. A cryptodome intrusion causing an uplift of the Puy Grosmanaux scoria cone and possibly associated to Kilian eruption (Van Wyk de Vries et al. 2014) is here omitted for simplicity

sealing of the pores by cristobalite, or (iv) granular densification during sintering. Several studies suggested that occlusion of pore space by vapor-phase precipitation of cristobalite can cause a reduction in permeability, promoting gas pressurization and destabilization of the dome and explosive activity (Horwell et al. 2013; Boudon et al. 2015). The Type 2 dome pyroclasts containing cristobalite have a permeability ranging between 10^{-16} and 10^{-12} m^2 (Colombier et al. 2017a) implying that the presence of cristobalite is not systematically linked with complete densification in the Kilian domes. We propose that additional processes such as sintering, compaction, pore collapse, and/or limited pre-fragmentation coalescence (e.g., Okumura et al. 2013; Kendrick et al. 2016; Wadsworth et al. 2017; Von Aulock et al. 2017; Ryan et al. 2018) also contributed to the reduction of permeability within the conduit.

Magma ascent and rheological changes during the 9.4 ka eruption

The eruption started with ascent of a low viscosity, trachytic magma with a temperature T_i ~ 775 °C and an initial water content of 8 wt% from a depth corresponding to a lithosthatic pressure of 300–400 MPa (Martel et al. 2013). These conditions imply an initial melt viscosity of $10^{1.71}$ Pa.s. Magma ascent from this reservoir was marked by a (i) significant increase in melt viscosity up to $10^{11.07}$ Pa.s at the time of quenching of vesicular magma (that is, at the glass transition temperature T_g) in the conduit at shallow levels, and (ii) a dramatic loss of H_2O from 8 wt% to 0.04 wt% inferred from the viscosity model and thermogravimetric analysis. Before quenching to the glass transition, the viscosity of the trachytic melt in the pumice population assuming isothermal decompression at 775 °C was $10^{9.38}$ Pa.s. We note that fragmentation of the vesicular magma may have occurred at or above T_g giving a temperature range of 689–775 °C. Decompression-induced crystallization and the ensuing rise in melt SiO_2 contributed to increasing the melt viscosity significantly. Melt viscosity calculated using the Giordano et al. (2008) model is even higher in the dome core due to more extensive crystallization and evolution towards rhyolitic composition (Fig. 5) with a value of $10^{11.69}$ Pa.s at 775 °C. In addition, the high crystal abundances in the magma likely increased the magma bulk viscosity significantly. We suggest that these strong rheological changes, coupled to efficient outgassing, were responsible for Vulcanian activity at Kilian Volcano.

Such extensive crystallization (Fig. 6) and water loss estimates agree with previous studies suggesting that both of these processes are relatively rapid in trachytic melts (e.g., Arzilli and Carroll 2013; Fanara et al. 2013; Shea et al. 2017; Arzilli et al. 2020). Effusive and explosive events in andesitic and rhyolitic magmas are typically associated with ascent rates lower and higher than approximately 3.6 MPa h^{-1}, respectively (Cassidy et al. 2018). We compiled crystallinity data as a function of depth from isothermal decompression experiments of crystallization at decompression rates that are faster and slower, respectively, than the explosive-effusive limit of 3.6 MPa h^{-1} (Hammer and Rutherford 2002; Szramek et al. 2006; Mollard et al. 2012; Arzilli and Carroll 2013; Martel and Iacono-Marziano 2015). We find an increase in the range and maximum value of crystallinity at shallow depth (< 3 km) with decreasing decompression rate for rhyolitic and basaltic-andesitic starting compositions (Fig.

11). We also find that the range of experimental microlite content at fast decompression rates and at shallow depth (< 3 km) straddles the natural data for sub-Plinian to Plinian explosive eruptions and obsidian flows with microlite content typically lower than 50 vol% (Fig. 11; Fig. 12e). On the other hand, microlite contents for slow decompression experiments at shallow range from 5 to 100 vol% and match data for volcanic rocks from Vulcanian eruptions and crystal-rich lava domes and plugs (Figs. 11 and 12e). This suggests that slow ascent rates are required for the effusive emplacement of crystal-rich lava domes/plugs, potentially followed by Vulcanian activity. Interestingly, the crystallinity in rapidly decompressed trachyte is higher than in rapidly decompressed basaltic-andesites and rhyolites with high crystallinities reached at shallow depth (Fig. 11; Fig. SM1 in the Supplementary Material). This may imply (i) that the effusive-explosive limit may be shifted to higher decompression rates for trachytic magmas and (ii) that initially fast trachytic magmas can lead to effusive or transient Vulcanian eruptive style due to efficient microlite crystallization during magma ascent followed by stagnation of the magma column favoring outgassing, cooling, and further crystallization. We note that the crystallinity profiles for experiments presented in Fig. 11 are also influenced by additional parameters such as variable temperatures, dwelling time at final pressure, and the experimental procedure to reach this final pressure (single-step vs. continuous decompression; Gaunt et al. 2020). However, the decompression rate appears to be a major control of the near-surficial crystallinity range attained.

We compare these dynamic, disequilibrium crystallization experiments to crystallinity profiles as a function of depth calculated at equilibrium conditions (i.e., independent of kinetics) using Rhyolite-MELTS (Gualda et al. 2012). The model was run using a representative average starting bulk composition (excluding the Type 2 dome pyroclasts with cristobalite, see Table 2), and storage conditions of 350 MPa, 8 wt% H_2O and assuming isothermal decompression with a range of temperature of 755–795 °C (see Martel et al. 2013). The isothermal assumption was based on the fact that cooling was limited to a maximum of 100 °C before crossing the glass transition temperature and that heating related to latent heat of crystallization or friction is limited or localized to zones of high strain localization (Blundy et al. 2006; Lavallée et al. 2015). Rhyolite-MELTS runs yield crystallinities similar to the natural case for Kilian trachytes at deep (storage) and surficial (dome carapace) conditions (Fig. 11). The modelled values also compare nicely with some decompression experiments at shallow depths. However, the crystallinity profile calculated by

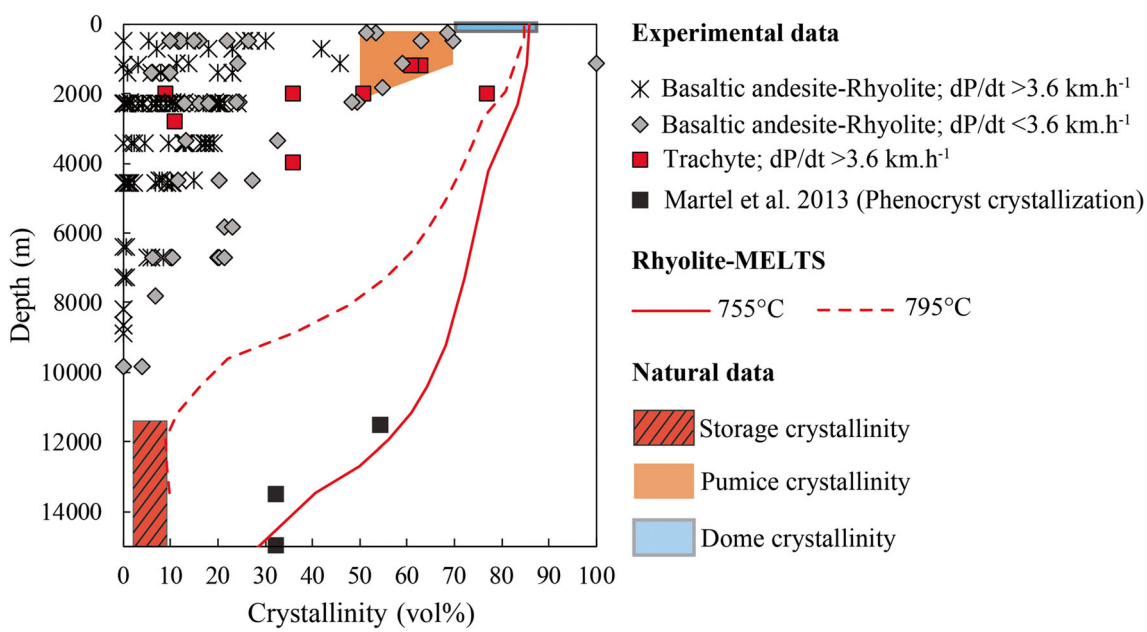

Fig. 11 Evolution of crystallinity with depth from storage region to atmospheric pressure during the Kilian dome-forming, Vulcanian phases. The experimental data correspond to isothermal decompression-induced crystallization experiments on basaltic-andesitic and rhyolitic melts with fast (> 3.6 MPa h^{-1}) and slow (< 3.6 MPa h^{-1}) decompression rates, respectively, and on trachytes at fast decompression rate (> 3.6 MPa h^{-}). Equilibrium crystallization conditions are shown with a modelled crystallinity profile using Rhyolite-MELTS at 755 °C and 795 °C and by crystallization experiments at storage conditions of Martel et al. (2013). The shaded areas correspond to the depth-crystallinity conditions for the storage region (Martel et al. 2013; Colombier et al. 2017a), the pumice population, and lava dome (few hundred meters thick and with its surface at atmospheric pressure). A hypothetical range of depth is illustrated for the magma underlying the lava dome (pumice population) by matching the minimum and maximum crystallinity observed in the pumice pyroclasts with similar experimental values obtained for trachytes by Arzilli and Caroll (2013). Error bars for crystallinity are given in figure SM1 in the Supplementary Material

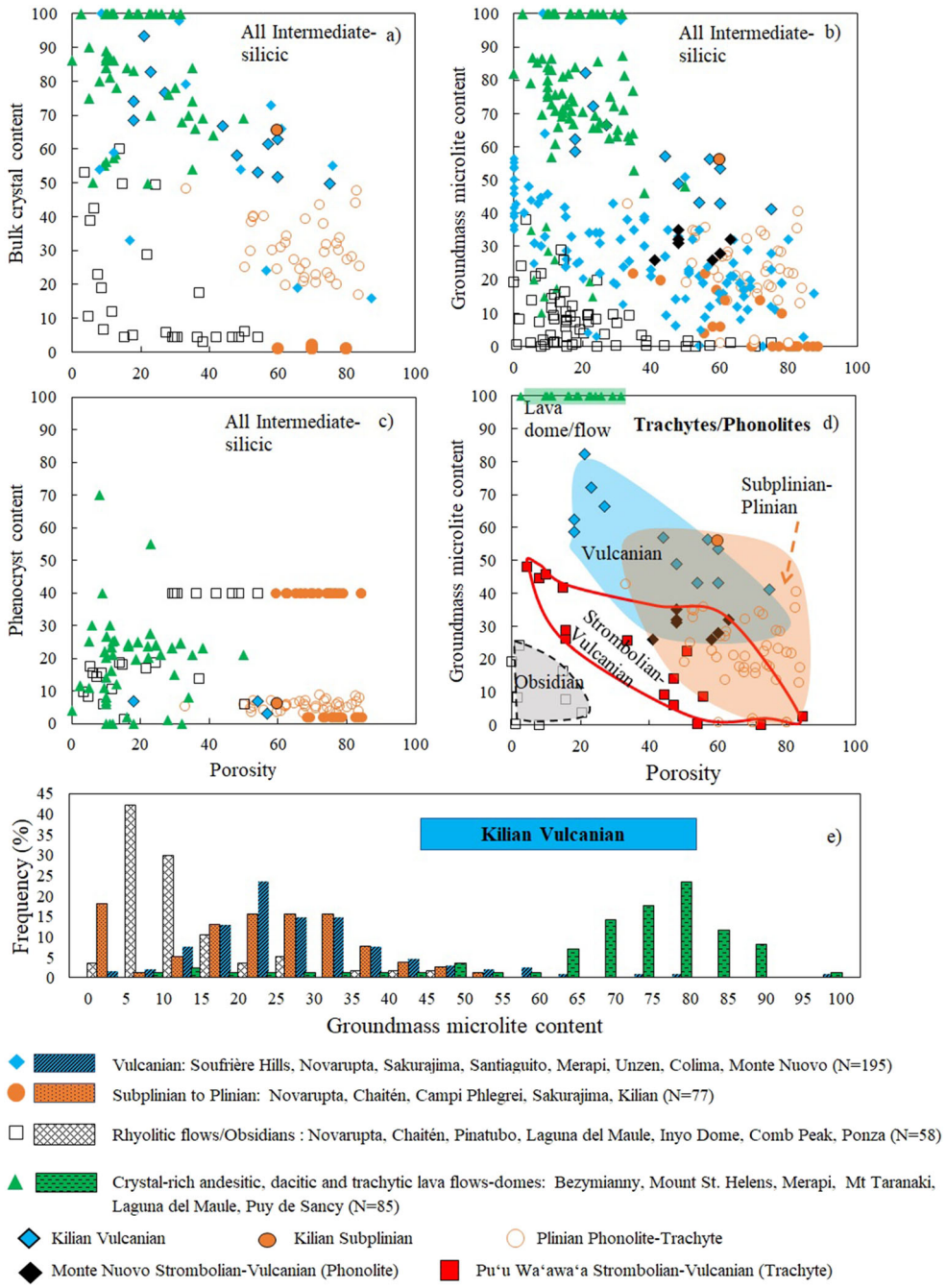

Fig. 12 Compilation of porosity and bulk, microlite, and phenocryst contents for silicic volcanic rocks of different eruptive styles. **a**–**c** All compositions are included. **d** Only microlite data for trachytes and phonolites are shown. **e** Frequency histogram showing the distribution of microlite content for the different eruptive styles and highlighting the absence of low microlite content at Kilian compared to sub alkaline Vulcanian eruptions. N is the total number of pyroclasts analyzed from the different studies included in the frequency histogram. To allow comparison between all the different studies, microlite contents were corrected from phenocryst content and porosity when needed and therefore correspond to groundmass microlite contents.

MELTS at intermediate depth (3–8 km) is significantly larger than the values obtained by decompression experiments. As a result, we interpret the crystallinity trends of the Kilian magma primarily in light of experimental data.

We infer that the Kilian magmas experienced high initial decompression rates (due to the initial low magma viscosity and high water content) which favored disequilibrium conditions. The fast crystallization of trachytic magma was nevertheless high enough for crystallization to keep pace with this rapid ascent, yielding high final crystallinities at a shallow depth in the conduit (< 2 km; Fig. 11). Crystallization progressively hindered ascent and caused magma stalling at the level of the plug or dome and of the underlying vesicular magma. Assuming that the decompression rate of the volatile-rich trachytic magma was similar to the experimental rate of trachytic melt at 7–60 MPa h^{-1}, we obtain a time scale of 5 to 57 h for replenishment of the conduit and shallow emplacement of the dome and underlying vesicular magma. These ascent rates are considerably higher than those estimated for other Vulcanian eruptions at Soufrière Hills (Montserrat) and Guagua Pichincha (Ecuador) volcanoes (~ 0.5–2 MPa h^{-1}; Druitt et al. 2002; Wright et al. 2007).

Generalization to trachytic volcanic eruptions

Small to moderate volume trachytic eruptions are often characterized by shifts in eruptive style such as dome-forming to Vulcanian styles (Kilian episodes U1, K1, and K2; Colombier et al. 2017a), Vulcanian to sub-Plinian styles (Kilian episodes U2 and U3; Colombier et al. 2017a), phreatomagmatic to Strombolian to Vulcanian (Monte Nuovo upper member, Phlegrean Fields, Italy; D'Oriano et al. 2005; Piochi et al. 2008), and obsidian dome- or plug-forming to Strombolian and Vulcanian styles (Pu'u Wa'awa'a, Hualālai volcano, Hawaii; Shea et al. 2017). On the other hand, large-volume, highly explosive eruptions of trachytic magma like the Plinian phase of the Campanian Ignimbrite eruption in the Phlegrean Fields, Italy, or the Povaçao ignimbrite in Azores, also occur (Rosi et al. 1999; Gottsmann et al. 2002; Polacci et al. 2003). This broad spectrum of eruptive style for trachytic magmas, even during a single eruption, is likely related to (i) the low viscosity of trachyte compared to rhyolite (Giordano et al. 2004; Andújar and Scaillet 2012), (ii) a slightly higher melt water diffusivity of trachytic magma compared to rhyolitic composition (Fanara et al. 2013), and (iii) the faster crystallization kinetics of trachytic magmas (e.g., D'Oriano et al. 2005; Arzilli and Caroll 2013; Shea et al. 2017; Arzilli et al. 2020). These idiosyncrasies cause first-order rheological changes in the magma and affect ascent rate, closed-system degassing, outgassing efficiency, and fragmentation behavior.

We compiled crystallinity and porosity data from the literature on intermediate to silicic volcanic rocks with a broad range of compositions and eruptive style (Fig. 12; Christiansen and Lipman 1966; Hammer et al. 1999; Nakamura 2006; Adams et al. 2006; Mastrolorenzo and Pappalardo 2006; Clarke et al. 2007; Lavallée et al. 2007; Noguchi et al. 2008; Piochi et al. 2008; Castro and Dingwell 2009; Miwa et al. 2009; Castro and Dingwell 2009; Neill et al. 2010; Giachetti et al. 2010; Burgisser et al. 2010; Shea et al. 2012; Scott et al. 2012; Miwa et al. 2013; Innocenti et al. 2013; Nguyen et al. 2014; Rotella et al. 2014; Cassidy et al. 2015; Preece et al. 2016; Hughes et al. 2017; Latutrie et al. 2017; Colombier et al. 2017a; Shea et al. 2017; Rangel et al. 2018; Zorn et al. 2018; Cáceres et al. 2018; this study). We separated the crystallinity datasets in terms of crystallinity, groundmass microlite content, and phenocryst content. When using the bulk and microlite contents (but not phenocryst contents), this compilation allows discrimination between pyroclasts of Plinian origin, Vulcanian origin, crystal-rich domes or plugs (and associated block-and-ash flows), and crystal-poor obsidian-bearing domes and flows. This implies that microlite content controls the crystallinity trends observed.

The tephra from Vulcanian eruptions range from relatively microlite-poor (microlite content < 50 vol%) pumice pyroclasts similar to those of Plinian eruptions to microlite-rich dome and plug material, with an anticorrelation and a kink in the crystallinity–porosity trend (Fig. 12b,e). The Kilian trachytes show a similar pattern but correspond to the upper bound of microlite content of this Vulcanian trend (Fig. 12b,e). In particular, microlite-poor pyroclasts (microlite content < 40 vol%) which are ubiquitous in the case of subalkaline Vulcanian eruptions are absent at Kilian Volcano. In general, we noticed that trachytic and phonolitic vesicular pyroclasts from Vulcanian to Plinian activity have a broader range of microlite content and are frequently microlite-richer than their subalkaline counterparts at a given porosity, which likely reflects the propensity of alkaline magmas to crystallize faster during ascent (Fig. 12b).

Comparing the datasets of microlite content for trachytic and phonolitic compositions offers valuable insights into potential end members of eruptive styles involving these compositions (Fig. 12d). A Vulcanian trachytic eruption involves the formation of a crystal-rich plug or dome via extensive crystallization and outgassing—a process which is possible even at ascent rates faster (i.e., higher than 3.6 MPa h^{-1}) than those inferred for dome-forming eruptions involving rhyolitic and andesitic compositions. In a scenario in which ascent is significantly faster and/or the temperature is higher, trachytic magmas may ascend without significant crystallization and erupt effusively as low viscosity obsidian plugs, domes, or flows, provided that outgassing is sufficiently efficient (Fig. 12d; Iezzi et al. 2008; Shea et al. 2017). On the other hand, at conditions of ascent rate, outgassing, and crystallization intermediate between the Vulcanian eruptive style observed at Kilian and obsidian-forming eruptions, trachytic magmas may switch between Strombolian and Vulcanian styles, as observed at Pu'u Wa'awa'a volcano (Shea et al. 2017). In such case, the tephra also displays a bimodal porosity distribution (Shea et al. 2017) and an anticorrelation of crystallinity with porosity (Fig. 12d). Finally, conditions for sub-Plinian to Plinian eruptions may be met for a range of microlite content from ~ 0 (e.g., Campanian Ignimbrite) to up to > 40 vol% (e.g., Kilian intermediate phases, Vesuvius) depending on ascent rate, melt viscosity and outgassing efficiency. The key observation of this compilation is that the eruptive style for a given trachytic or phonolitic magma will largely depend on the balance between the initial lower viscosity compared to subalkaline magmas and the faster crystallization of microlites in the conduit during magma ascent.

Implications for the cyclicity of trachytic-phonolitic Vulcanian eruptions

As discussed previously, trachytes are characterized by a broad spectrum of eruptive styles, with frequent effusive-explosive transitions that depend mainly on ascent rate, temperature, initial volatile content, crystallization kinetics, and outgassing efficiency prior to eruption. In particular, high ascent rates may be compensated by rapid crystallization causing magma stagnation and transient, cyclic Vulcanian

eruptions. Although these eruptions bear many similarities with Vulcanian eruptions involving andesitic and dacitic magmas (e.g., Soufrière Hills), we suggest that the main difference may be the shorter time for conduit replenishment in the case of trachytic magma. This may influence the cyclicity of these Vulcanian eruptions, with likely shorter intervals between explosive pulses than observed at well-monitored andesitic and dacitic volcanoes. We concur with the postulation of D'Oriano et al. (2005) that the balance between low viscosity and high crystal growth rates may shorten the time required for pressure build up during crystallization of evolved alkaline magmas. This, coupled to the paucity of observed trachytic and phonolitic eruptions, has implications for the hazard assessment of future activity at alkaline volcanoes.

Conclusion

This study is an attempt to shed light on the effusive-explosive transitions during Vulcanian episodes of the 9.4 ka eruption of Kilian Volcano, Chaîne des Puys, France and on trachytic eruptions in general. The principal conclusions are as follows:

- Initial effusive activity at Kilian Volcano was induced by rheological changes due to extensive microlite crystallization causing a magma viscosity increase of up to more than 10 orders of magnitude, and efficient closed- and open-system degassing.
- Outgassing occurred via bubble coalescence, brittle fracturing, and through tuffisite veins sintered following gas- and ash-explosions.
- Effusive activity transitioned to explosive Vulcanian episodes due to pressurization of the dome or of the underlying vesicular magma. Processes likely to have promoted overpressure and fragmentation during the explosive phases include limited pre-fragmentation bubble coalescence and outgassing in the hot vesicular magma underneath the lava dome, bubble collapse and reduction of permeability in the dome, sealing of the pores by cristobalite, and granular densification during sintering.
- The conduit prior to each Vulcanian explosion was stratified as reflected in the pyroclasts population with a transition from crystal-rich dome pyroclasts (carapace and talus regions) to glass-bearing dome pyroclasts (dome interior) and to pumice pyroclasts (underlying vesicular magma). This lithologic sequence and conduit stratigraphy are similar to those observed at Soufrière Hills volcano, Montserrat.
- Specific properties of trachytic magmas such as high water solubility, high water diffusivity, rapid crystal growth, and low viscosity yield a wide spectrum of rheology and degassing conditions. This promotes a broad range of eruptive style and frequent effusive-explosive transitions.

Although trachytic eruptions can jeopardize highly populated areas, the eruptive processes at these volcanoes remain less constrained than their subalkaline counterparts due to the paucity of direct observations of trachytic eruptions. Future studies will be necessary to better constrain the kinetics and coupled effect of vesiculation and crystallization processes and associated textures during decompression of trachytic magmas.

Supplementary Information The online version contains supplementary material available at https://doi.org/10.1007/s00445-020-01420-5.

Acknowledgments This work benefited from thoughtful comments and suggestions by the two reviewers Jessica Larsen and Hugh Tuffen that helped to significantly improve our manuscript. We are thankful to the executive editor Jacopo Taddeucci and the associate editor Michael James for editorial handling and additional comments on our manuscript. This is Laboratory of Excellence ClerVolc publication number 444.

Funding Open Access funding enabled and organized by Projekt DEAL. This study received support from an ERC ADG 2018 834225 (EAVESDROP).

Open Access This article is licensed under a Creative Commons Attribution 4.0 International License, which permits use, sharing, adaptation, distribution and reproduction in any medium or format, as long as you give appropriate credit to the original author(s) and the source, provide a link to the Creative Commons licence, and indicate if changes were made. The images or other third party material in this article are included in the article's Creative Commons licence, unless indicated otherwise in a credit line to the material. If material is not included in the article's Creative Commons licence and your intended use is not permitted by statutory regulation or exceeds the permitted use, you will need to obtain permission directly from the copyright holder. To view a copy of this licence, visit http://creativecommons.org/licenses/by/4.0/.

References

Adams NK, Houghton BF, Fagents SA, Hildreth W (2006) The transition from explosive to effusive eruptive regime: the example of the 1912 Novarupta eruption, Alaska. Bull Geol Soc Am 118:620–634. https://doi.org/10.1130/B25768.1

Andújar J, Scaillet B (2012) Relationships between pre-eruptive conditions and eruptive styles of phonolite – trachyte magmas. LITHOS 152:122–131. https://doi.org/10.1016/j.lithos.2012.05.009

Arzilli F, Carroll MR (2013) Crystallization kinetics of alkali feldspars in cooling and decompression-induced crystallization experiments in trachytic melt. Contrib Mineral Petrol 166:1011–1027. https://doi.org/10.1007/s00410-013-0906-1

Arzilli F, Stabile P, Fabbrizio A, Landi P, Scaillet B, Paris E, Carroll MR (2020) Crystallization kinetics of Alkali Feldspar in peralkaline rhyolitic melts : implications for Pantelleria Volcano. Front Earth Sci 8: 177. https://doi.org/10.3389/feart.2020.00177

Belousov A, Behncke B, Belousova M (2011) Generation of pyroclastic flows by explosive interaction of lava flows with ice / water-saturated substrate. J Volcanol Geotherm Res 202:60–72. https://doi.org/10.1016/j.jvolgeores.2011.01.004

Blower J (2001) Factors controlling permeability-porosity relationships in magma. Bull Volcanol 63:497–504. https://doi.org/10.1007/s004450100172

Blundy J, Cashman K (2001) Ascent-driven crystallisation of dacite magmas at Mount St Helens, 1980–1986. Contrib Mineral Petrol 2:631–650. https://doi.org/10.1007/s004100000219

Blundy J, Cashman K, Humphreys M (2006) Magma heating by decompression-driven crystallization beneath andesite volcanoes. Nature 443:76–80. https://doi.org/10.1038/nature05100

Boivin P, Thouret JC (2014) The Volcanic Chaîne des Puys: a unique collection of simple and compound monogenetic edifices. In: Fort M, André MF (eds) Landscapes and Landforms of France. World Geomorphological Landscapes. Springer, Dordrecht, pp 81–91. https://doi.org/10.1007/978-94-007-7022-5_9

Boivin P, Miallier D, Cluzel N, Devidal JL, Dousteyssier B (2015) Building and ornamental use of trachyte in the center of France during antiquity : sources and criteria of identification. J Archaeol Sci Rep 3:247–256. https://doi.org/10.1016/j.jasrep.2015.06.017

Boivin P, Besson JC, Briot D, Deniel C, Gourgaud A, Labazuy P, Langlois E, Larouzière FD de, Livet M, Merciecca C, Médard E, Mergoil J, Miallier D, Morel JM, Thouret JC, Vernet G (2017) Volcanologie de la Chaîne des Puys Massif Central Français. 6e édition, bilingue. Édition Parc Naturel Régional des Volcans d'Auvergne Château de Montlosier, Randanne, 63970 Aydat. 200 p. Carte 1/25 000, 120x90 cm

Boudon G, Balcone-boissard H, Villemant B, Morgan DJ (2015) What factors control superficial lava dome explosivity ? Sci Rep 5:1–14. https://doi.org/10.1038/srep14551

Burgisser A, Poussineau S, Arbaret L et al (2010) Pre-explosive conduit conditions of the 1997 Vulcanian explosions at Soufrière Hills Volcano, Montserrat : I . pressure and vesicularity distributions. J Volcanol Geotherm Res 194:27–41. https://doi.org/10.1016/j.jvolgeores.2010.04.008

Cáceres F, Castruccio Á, Parada MA (2018) Morphology , effusion rates and petrology of postglacial lavas of Laguna del Maule Volcanic Field , Chilean Andes , and implications for their plumbing system. Geochem Geophys Geosyst 19:4925–4944. https://doi.org/10.1029/2018GC007817

Cáceres F, Wadsworth FB, Scheu B, Colombier M, Madonna C, Cimarelli C, Hess KU, Kaliwoda M, Ruthensteiner B, Dingwell DB (2020) Can nanolites enhance eruption explosivity? Geology 48:997–1001. https://doi.org/10.1130/G47317.1

Calder ES, Lavallée Y, Kendrick JE, Bernstein M (2015) Lava dome eruptions. In: Sigurdsson, H (ed) The encyclopedia of volcanoes, 2nd edn. Academic Press, pp 343-362. https://doi.org/10.1016/B978-0-12-385938-9.00018-3

Cassidy M, Cole PD, Hicks KE, Varley NR, Peters N, Lerner AH (2015) Rapid and slow: varying magma ascent rates as a mechanism for Vulcanian explosions. Earth Planet Sci Lett 420:73–84. https://doi.org/10.1016/j.epsl.2015.03.025

Cassidy M, Manga M, Cashman K, Bachmann O (2018) Controls on explosive-effusive volcanic eruption styles. Nat Commun 9:1–6. https://doi.org/10.1038/s41467-018-05293-3

Castro JM, Dingwell DB (2009) Rapid ascent of rhyolitic magma at Chaitén volcano, Chile. Nature 461:780–783. https://doi.org/10.1038/nature08458

Castro JM, Bindeman IN, Tuffen H, Schipper CI (2014) Explosive origin of silicic lava: Textural and δD-H_2O evidence for pyroclastic degassing during rhyolite effusion. Earth Planet Sci Lett 405:52–61. https://doi.org/10.1016/j.epsl.2014.08.012

Christiansen R, Lipman PW (1966) Emplacement and thermal history of a rhyolite lava flow near Fortymile Canyon , Southern Nevada. Geol Soc Am Bull 77:671–684. https://doi.org/10.1130/0016-7606(1966)77

Clarke AB, Stephens S, Teasdale R, Sparks RSJ, Diller K (2007) Petrologic constraints on the decompression history of magma prior to Vulcanian explosions at the Soufrière Hills volcano, Montserrat. J Volcanol Geotherm Res 161:261–274. https://doi.org/10.1016/j.jvolgeores.2006.11.007

Cluzel N, Laporte D, Provost A, Kannewischer I (2008) Kinetics of heterogeneous bubble nucleation in rhyolitic melts : implications for the number density of bubbles in volcanic conduits and for pumice textures. Contri 156:745–763. https://doi.org/10.1007/s00410-008-0313-1

Colombier M, Gurioli L, Druitt TH, Shea T, Boivin P, Miallier D, Cluzel N (2017a) Textural evolution of magma during the 9.4-ka trachytic explosive eruption at Kilian Volcano, Chaîne des Puys, France. Bull Volcanol 79. https://doi.org/10.1007/s00445-017-1099-7

Colombier M, Wadsworth FB, Gurioli L, Scheu B, Kueppers U, di Muro A, Dingwell DB (2017b) The evolution of pore connectivity in volcanic rocks. Earth Planet Sci Lett 462:99–109. https://doi.org/10.1016/j.epsl.2017.01.011

Colombier M, Wadsworth FB, Scheu B, Vasseur J, Dobson KJ, Cáceres F, Allabar A, Marone F, Schlepütz CM, Dingwell DB (2020) In situ observation of the percolation threshold in multiphase magma analogues. Bull Volcanol 82:1–15. https://doi.org/10.1007/s00445-020-1370-1

Couch S, Harford CL, Sparks RSJ, Carroll MR (2003) Experimental constraints on the conditions of formation of highly Calcic Plagioclase Microlites at the Soufrière Hills, Montserrat. J Petrol 44:1455–1475. https://doi.org/10.1093/petrology/44.8.1455

D'Oriano C, Poggianti E, Bertagnini A, Cioni R, Landi P, Polacci M, Rosi M (2005) Changes in eruptive style during the A .D. 1538 Monte Nuovo eruption (Phlegrean Fields , Italy): the role of syn-eruptive crystallization. Bull Volcanol 67:601–621. https://doi.org/10.1007/s00445-004-0397-z

Damby DE, Llewellin EW, Horwell CJ, Williamson BJ, Najorka J, Cressey G, Carpenter M (2014) The α–β phase transition in volcanic cristobalite. J Appl Crystallogr 47:1205–1215. https://doi.org/10.1107/S160057671401070X

de Andrade FRD, Polo LA, Janasi V d A, Carvalho FMS (2017) Volcanic glass in Cretaceous dacites and rhyolites of the Paraná Magmatic Province , southern Brazil : characterization and quantification by XRD- Rietveld. J Volcanol Geotherm Res 355:219–231. https://doi.org/10.1016/j.jvolgeores.2017.08.008

De Hoog JCM, Van Bergen MJ, Jacobs MHG (2005) Vapour-phase crystallisation of silica from SiF4 -bearing volcanic gases. Ann Geophys 48:775–785. https://doi.org/10.4401/ag-3233

Delcamp A, Van Wyk De Vries B, Stéphane P, Kervyn M (2014) Endogenous and exogenous growth of the monogenetic Lemptégy volcano in. Geol Soc Am 10:998–1019. https://doi.org/10.1130/GES01007.1

Deniel C, Boivin P, Miallier D, Gerbe MC (2020) Multi-stage growth of the trachytic lava dome of the Puy de Dôme (Chaîne des Puys, France). Field, geomorphological and petro-geochemical evidence. J Volcanol Geotherm Res 396:106749. https://doi.org/10.1016/j.jvolgeores.2019.106749

Di Matteo V, Carroll MR, Behrens H et al (2004) Water solubility in trachytic melts. Chem Geol 213:187–196. https://doi.org/10.1016/j.chemgeo.2004.08.042

Dingwell DB, Hess KU (1998) Melt viscosities in the system Na-Fe-Si-O-F-Cl: Contrasting effects of F and Cl in alkaline melts. Am Mineral 83:1016–1021

Döbelin N, Kleeberg R (2015) Profex: a graphical user interface for the Rietveld refinement program BGMN. J Appl Crystallogr 48:1573–1580. https://doi.org/10.1107/S1600576715014685

Druitt TH, Young SR, Baptie B, Bonadonna C, Calder ES, Clarke AB, Cole PD, Harford CL, Herd RA, Luckett R, Ryan G, Voight B (2002) Episodes of cyclic Vulcanian explosive activity with fountain collapse at Soufrière Hills Volcano , Montserrat. Geol Soc Lond Mem 21:281–306. https://doi.org/10.1144/GSL.MEM.2002.021.01.13

Dunn TL, Cressey G, McSween HY Jr, McCoy TJ (2010) Analysis of ordinary chondrites using powder X-ray diffraction : 1 . Modal mineral abundances. Meteorit Planet Sci 45:123–134. https://doi.org/10.1111/j.1945-5100.2009.01011.x

Eichelberger JC, Carrigan CR, Westrich HR, Price RH (1986) Non-explosive silicic volcanism. Nature 323:598–602. https://doi.org/10.1038/323598a0

Fanara S, Behrens H, Zhang Y (2013) Water diffusion in potassium-rich phonolitic and trachytic melts. Chem Geol 346:149–161. https://doi.org/10.1016/j.chemgeo.2012.09.030

Fitch EP, Fagents SA, Thordarson T, Hamilton CW (2017) Fragmentation mechanisms associated with explosive lava–water interactions in a lacustrine environment. Bull Volcanol 79:12. https://doi.org/10.1007/s00445-016-1087-3

Formenti Y, Druitt TH (2003) Vesicle connectivity in pyroclasts and implications for the fluidisation of fountain-collapse pyroclastic flows, Montserrat (West Indies). Earth Planet Sci Lett 214:561–574. https://doi.org/10.1016/S0012-821X(03)00386-8

Forte P, Castro JM (2019) H_2O-content and temperature limit the explosive potential of rhyolite magma during Plinian eruptions. Earth Planet Sci Lett 506:157–167. https://doi.org/10.1016/j.epsl.2018.10.041

Gaunt HE, Sammonds PR, Meredith PG, Smith R, Pallister JS (2014) Pathways for degassing during the lava dome eruption of Mount St . Helens 2004 – 2008. Geology 42:947–950. https://doi.org/10.1130/G35940.1

Gaunt HE, Burgisser A, Mothes PA, Browning J, Meredith PG, Criollo E, Bernard B (2020) Triggering of the powerful 14 July 2013 Vulcanian explosion at Tungurahua Volcano, Ecuador. J Volcanol Geotherm Res 106762:106762. https://doi.org/10.1016/j.jvolgeores.2019.106762

Giachetti T, Druitt TH, Burgisser A, Arbaret L, Galven C (2010) Bubble nucleation, growth and coalescence during the 1997 Vulcanian explosions of Soufrière Hills Volcano, Montserrat. J Volcanol Geotherm Res 193:215–231. https://doi.org/10.1016/j.jvolgeores.2010.04.001

Giachetti T, Gonnermann HM, Gardner JE, Shea T, Gouldstone A (2015) Discriminating secondary from magmatic water in rhyolitic matrix-glass of volcanic pyroclasts using thermogravimetric analysis. Geochim Cosmochim Acta 148:457–476. https://doi.org/10.1016/j.gca.2014.10.017

Giordano D, Romano C, Papale P, Dingwell DB (2004) The viscosity of trachytes, and comparison with basalts, phonolites, and rhyolites. Chem Geol 213:49–61. https://doi.org/10.1016/j.chemgeo.2004.08.032

Giordano D, Russell JK, Dingwell DB (2008) Viscosity of magmatic liquids : a model. Earth Planet Sci Lett 271:123–134. https://doi.org/10.1016/j.epsl.2008.03.038

Gottsmann J, Giordano D, Dingwell DB (2002) Predicting shear viscosity during volcanic processes at the glass transition: a calorimetric calibration. Earth Planet Sci Lett 198:417–427. https://doi.org/10.1016/S0012-821X(02)00522-8

Gualda GAR, Ghiorso MS, Lemons RV, Carley TL (2012) Rhyolite-MELTS: a modified calibration of MELTS optimized for silica-rich , fluid-bearing magmatic systems. J Petrol 53:875–890. https://doi.org/10.1093/petrology/egr080

Hammer JE, Rutherford MJ (2002) An experimental study of the kinetics of decompression-induced crystallization in silicic melt. J Geophys Res 107:107–ECV 8-24. https://doi.org/10.1029/2001JB000281

Hammer JE, Cashman KV, Hoblitt RP, Newman S (1999) Degassing and microlite crystallization during pre-climactic events of the 1991 eruption of Mt. Pinatubo, Philippines. Bull Volcanol 60:355–380. https://doi.org/10.1007/s004450050238

Harford CL, Sparks RSJ, Fallick AE (2003) Degassing at the Soufrière Hills Volcano, Montserrat , recorded in matrix glass compositions. J Petrol 44:1503–1523. https://doi.org/10.1093/petrology/44.8.1503

Harnett CE, Thomas ME, Purvance MD, Neuberg J (2018) Using a discrete element approach to model lava dome emplacement and collapse. J Volcanol Geotherm Res 359:68–77. https://doi.org/10.1016/j.jvolgeores.2018.06.017

Heap MJ, Coats R, Chen C, Varley N, Lavallée Y, Kendrick J, Xu T, Reuschlé T (2018) Thermal resilience of microcracked andesitic dome rocks. J Volcanol Geotherm Res 367:20–30. https://doi.org/10.1016/j.jvolgeores.2018.10.021

Heap MJ, Tuffen H, Wadsworth FB, Reuschlé T, Castro JM, Schipper CI (2019) The permeability evolution of tuffisites and implications for outgassing through dense rhyolitic magma. J Geophys Res Solid Earth 124:8281–8299. https://doi.org/10.1029/2018JB017035

Heinrich M, Cronin SJ, Torres-orozco R et al (2020) Micro-porous pyroclasts reflecting multi-vent basaltic-andesite Plinian eruptions at Mt. Tongariro , New Zealand. J Volcanol Geotherm Res 401:106936. https://doi.org/10.1016/j.jvolgeores.2020.106936

Horwell CJ, Williamson BJ, Llewellin EW, Damby DE, le Blond JS (2013) The nature and formation of cristobalite at the Soufrière Hills volcano, Montserrat : implications for the petrology and stability of silicic lava domes. Bull Volcanol 75. https://doi.org/10.1007/s00445-013-0696-3

Hughes EC, Neave DA, Dobson KJ, Withers PJ, Edmonds M (2017) How to fragment peralkaline rhyolites : observations on pumice using combined multi-scale 2D and 3D imaging. J Volcanol Geotherm Res 336:179–191. https://doi.org/10.1016/j.jvolgeores.2017.02.020

Iezzi G, Mollo S, Ventura G, Cavallo A, Romano C (2008) Experimental solidification of anhydrous latitic and trachytic melts at different cooling rates : the role of nucleation kinetics. Chem Geol 253:91–101. https://doi.org/10.1016/j.chemgeo.2008.04.008

Innocenti S, Andreastuti S, Furman T, del Marmol MA, Voight B (2013) The pre-eruption conditions for explosive eruptions at Merapi volcano as revealed by crystal texture and mineralogy. J Volcanol Geotherm Res 261:69–86. https://doi.org/10.1016/j.jvolgeores.2012.12.028

Jaupart C, Allègre CJ (1991) Gas content, eruption rate and instabilities of eruption regime in silicic volcanoes. Earth Planet Sci Lett 102:413–429. https://doi.org/10.1016/0012-821X(91)90032-D

Juvigné E, Kroonenberg S, Veldkamp A, el Arabi A, Vernet G (1992) Widespread Alleröd and boreal trachyandesitic to trachytic tephra layers as stratigraphical markers in the Massif Central, France. Quaternaire 3:137–146

Kendrick JE, Lavallée Y, Varley NR, Wadsworth FB, Lamb OD, Vasseur J (2016) Blowing off steam: tuffisite formation as a regulator for lava dome eruptions. Front Earth Sci 4:1–15. https://doi.org/10.3389/feart.2016.00041

Kolzenburg S, Heap MJ, Lavallée Y, Russell JK, Meredith PG, Dingwell DB (2012) Strength and permeability recovery of tuffisite-bearing andesite. Solid Earth 3:191–198. https://doi.org/10.5194/se-3-191-2012

Kushnir ARL, Martel C, Bourdier J et al (2016) Probing permeability and microstructure: unravelling the role of a low-permeability dome on the explosivity of Merapi (Indonesia). J Volcanol Geotherm Res 316:56–71. https://doi.org/10.1016/j.jvolgeores.2016.02.012

Lamur A, Kendrick JE, Eggertsson GH, Wall RJ, Ashworth JD, Lavallée Y (2017) The permeability of fractured rocks in pressurised volcanic and geothermal systems. Sci Rep 7:1–9. https://doi.org/10.1038/s41598-017-05460-4

Lane CS, Blockley SPE, Ramsey CB, Lotter AF (2011) Tephrochronology and absolute centennial scale synchronisation of European and Greenland records for the last glacial to interglacial transition: a case study of Soppensee and NGRIP. Quat Int 246:145–156. https://doi.org/10.1016/j.quaint.2010.11.028

Latutrie B, Andredakis I, Groeve TDE et al (2016) Testing a geographical information system for damage and evacuation assessment during

an effusive volcanic crisis. Geol Soc London, Spec Publ 426:649–672. https://doi.org/10.1144/SP426.19

Latutrie B, Harris A, Médard E, Gurioli L (2017) Eruption and emplacement dynamics of a thick trachytic lava flow of the Sancy volcano (France). Bull Volcanol 79. https://doi.org/10.1007/s00445-016-1084-6

Lavallée Y, Hess K, Cordonnier B, Dingwell DB (2007) Non-Newtonian rheological law for highly crystalline dome lavas. Geology 35:843–846. https://doi.org/10.1130/G23594A.1

Lavallée Y, Varley NR, Alatorre-Ibargüengoitia M et al (2012) Magmatic architecture of dome-building eruptions at Volcán. Bull Volcanol 74:249–260. https://doi.org/10.1007/s00445-011-0518-4

Lavallée Y, Benson PM, Heap MJ, Hess KU, Flaws A, Schillinger B, Meredith PG, Dingwell DB (2013) Reconstructing magma failure and the degassing network of dome- building eruptions. Geology 41:515–518. https://doi.org/10.1130/G33948.1

Lavallée Y, Dingwell DB, Johnson JB, Cimarelli C, Hornby AJ, Kendrick JE, von Aulock FW, Kennedy BM, Andrews BJ, Wadsworth FB, Rhodes E, Chigna G (2015) Thermal vesiculation during volcanic eruptions. Nature 528:544–547. https://doi.org/10.1038/nature16153

Le Bas MJ, Le Maitre RW, Streckeisen A, Zanettin B (1986) A chemical classification of volcanic rocks based on the total alkali-silica diagram. J Petrol 27:745–750. https://doi.org/10.1093/petrology/27.3.745

Lindoo A, Larsen JF, Cashman KV, Oppenheimer J (2017) Crystal controls on permeability development and degassing in basaltic andesite magma. Geol Soc Am 45:2–5. https://doi.org/10.1130/G39157.1

Martel C, Iacono-Marziano G (2015) Timescales of bubble coalescence, outgassing, and foam collapse in decompressed rhyolitic melts. Earth Planet Sci Lett 412:173–185. https://doi.org/10.1016/j.epsl.2014.12.010

Martel C, Champallier MI, Prouteau G et al (2013) Trachyte phase relations and implication for magma storage conditions in the Chaîne des Puys (French Massif Central). J Petrol 54:1071–1107. https://doi.org/10.1093/petrology/egt006

Mastrolorenzo G, Pappalardo L (2006) Magma degassing and crystallization processes during eruptions of high-risk Neapolitan-volcanoes : evidence of common equilibrium rising processes in alkaline magmas. Earth Planet Sci Lett 250:164–181. https://doi.org/10.1016/10.1016/j.epsl.2006.07.040

Miallier D, Pilleyre T, Sanzelle S, Boivin P, Lanos P (2012) Revised chronology of the youngest volcanoes of the Chaîne des Puys (French Massif Central). Quaternaire 23(4):283–290. https://doi.org/10.4000/quaternaire.6367

Miwa T, Toramaru A, Iguchi M (2009) Correlations of volcanic ash texture with explosion earthquakes from vulcanian eruptions at Sakurajima volcano, Japan. J Volcanol Geotherm Res 184:473–486. https://doi.org/10.1016/j.jvolgeores.2009.05.012

Miwa T, Geshi N, Shinohara H (2013) Temporal variation in volcanic ash texture during a vulcanian eruption at the Sakurajima volcano, Japan. J Volcanol Geotherm Res 260:80–89. https://doi.org/10.1016/j.jvolgeores.2013.05.010

Moitra P, Gonnermann HM, Houghton BF, Tiwary CS (2018) Fragmentation and Plinian eruption of crystallizing basaltic magma. Earth Planet Sci Lett 500:97–104. https://doi.org/10.1016/j.epsl.2018.08.003

Mollard E, Martel C, Bourdier J (2012) Decompression-induced crystallization in hydrated silica-rich melts : empirical models of experimental plagioclase nucleation and growth kinetics. J Petrol 53:1743–1766. https://doi.org/10.1093/petrology/egs031

Mueller S, Melnik O, Spieler O, Scheu B, Dingwell DB (2005) Permeability and degassing of dome lavas undergoing rapid decompression: an experimental determination. Bull Volcanol 67:526–538. https://doi.org/10.1007/s00445-004-0392-4

Mujin M, Nakamura M (2014) A nanolite record of eruption style transition. Geology 42:611–614. https://doi.org/10.1130/G35553.1

Nakamura K (2006) Textures of plagioclase microlite and vesicles within volcanic products of the 1914-1915 eruption of Sakurajima Volcano, Kyushu, Japan. J Mineral Petrol Sci 101:178–198. https://doi.org/10.2465/jmps.101.178

Neill OK, Hammer JE, Izbekov PE, Belousova MG, Belousov AB, Clarke AB, Voight B (2010) Influence of pre-eruptive degassing and crystallization on the juvenile products of laterally directed volcanic explosions. J Volcanol Geotherm Res 198:264–274. https://doi.org/10.1016/j.jvolgeores.2010.09.011

Noguchi S, Toramaru A, Nakada S (2008) Relation between microlite textures and discharge rate during the 1991 – 1995 eruptions at Unzen, Japan. J Volcanol Geotherm Res 175:141–155. https://doi.org/10.1016/j.jvolgeores.2008.03.025

Okumura S, Nakamura M, Uesugi K, Nakano T, Fujioka T (2013) Coupled effect of magma degassing and rheology on silicic volcanism. Earth Planet Sci Lett 362:163–170. https://doi.org/10.1016/j.epsl.2012.11.056

Oppenheimer J, Rust AC, Cashman KV, Sandnes B (2015) Gas migration regimes and outgassing in particle-rich suspensions. Front Phys 3:1–13. https://doi.org/10.3389/fphy.2015.00060

Parmigiani A, Faroughi S, Huber C, Bachmann O, Su Y (2016) Bubble accumulation and its role in the evolution of magma reservoirs in the upper crust. Nature 532:492–495. https://doi.org/10.1038/nature17401

Piochi M, Polacci M, De Astis G et al (2008) Texture and composition of pumices and scoriae from the Campi Flegrei caldera (Italy): implications on the dynamics of explosive eruptions. Geochem Geophys Geosyst 9. https://doi.org/10.1029/2007GC001746

Platz T, Cronin SJ, Cashman KV, Stewart RB, Smith IEM (2007) Transition from effusive to explosive phases in andesite eruptions - a case-study from the AD1655 eruption of Mt. Taranaki, New Zealand. J Volcanol Geotherm Res 161:15–34. https://doi.org/10.1016/j.jvolgeores.2006.11.005

Pleše P, Higgins MD, Mancini L, Lanzafame G, Brun F, Fife JL, Casselman J, Baker DR (2018) Dynamic observations of vesiculation reveal the role of silicate crystals in bubble nucleation and growth in andesitic magmas. Lithos 299:532–546. https://doi.org/10.1016/j.lithos.2017.11.024

Polacci M, Pioli L, Rosi M (2003) The Plinian phase of the Campanian Ignimbrite eruption (Phlegrean Fields , Italy): evidence from density measurements and textural characterization of pumice. Bull Volcanol 65:418–432. https://doi.org/10.1007/s00445-002-0268-4

Portal A, Gailler L, Labazuy P, Lénat J (2016) Geophysical imaging of the inner structure of a lava dome and its environment through gravimetry and magnetism. J Volcanol Geotherm Res 320:88–99. https://doi.org/10.1016/j.jvolgeores.2016.04.012

Portal A, Fargier Y, Labazuy P, Lénat JF, Boivin P, Miallier D (2019) 3D electrical imaging of the inner structure of a complex lava dome, Puy de Dôme volcano (French Massif Central, France). J Volcanol Geotherm Res 373:97–107. https://doi.org/10.1016/j.jvolgeores.2019.01.019

Preece K, Gertisser R, Barclay J, Charbonnier SJ, Komorowski JC, Herd RA (2016) Transitions between explosive and effusive phases during the cataclysmic 2010 eruption of Merapi volcano, Java, Indonesia. Bull Volcanol 78:54. https://doi.org/10.1007/s00445-016-1046-z

Rangel E, Arce JL, Macías JL (2018) Storage conditions of the ~ 29 ka rhyolitic Guangoche White Pumice Sequence, Los Azufres Volcanic Field, Central Mexico. J Volcanol Geotherm Res 358:132–148. https://doi.org/10.1016/j.jvolgeores.2018.03.016

Rosi M, Vezzoli L, Castelmenzano A, Grieco G (1999) Plinian pumice fall deposit of the Campanian Ignimbrite eruption (Phlegraean Fields, Italy). J Volcanol Geotherm Res 91:179–198. https://doi.org/10.1016/S0377-0273(99)00035-9

Rotella MD, Wilson CJN, Barker SJ, Cashman KV, Houghton BF, Wright IC (2014) Bubble development in explosive silicic eruptions : insights from pyroclast vesicularity textures from Raoul volcano (Kermadec arc). Bull Volcanol 76. https://doi.org/10.1007/s00445-014-0826-6

Rowe M, Ellis BS, Lindeberg A (2012) Quantifying crystallization and devitrification of rhyolites by means of X- ray diffraction and electron microprobe analysis. Am Mineral 97:1685–1699. https://doi.org/10.2138/am.2012.4006

Ryan A, Russell JK, Heap MJ (2018) Rapid solid-state sintering in volcanic systems. Am Mineral 103:2028–2031. https://doi.org/10.2138/am-2018-6714

Saubin E, Tuffen H, Gurioli L, Owen J, Castro JM, Berlo K, McGowan EM, Schipper CI, Wehbe K (2016) Conduit dynamics in transitional rhyolitic activity recorded by tuffisite vein textures from the 2008–2009 Chaitén Eruption. Front Earth Sci 4:4. https://doi.org/10.3389/feart.2016.00059

Schipper CI, Castro JM, Tuffen H, Wadsworth FB, Chappell D, Pantoja AE, Simpson MP, le Ru EC (2015) Cristobalite in the 2011 – 2012 Cordón Caulle eruption (Chile). Bull Volcanol 77. https://doi.org/10.1007/s00445-015-0925-z

Schipper CI, Mandon C, Maksimenko A et al (2017) Vapor-phase cristobalite as a durable indicator of magmatic pore structure and halogen degassing: an example from White Island volcano (New Zealand). Bull Volcanol 79. https://doi.org/10.1007/s00445-017-1157-1

Schipper CI, Castro JM, Kennedy BM, Christenson BW, Aiuppa A, Alloway B, Forte P, Seropian G, Tuffen H (2019) Halogen (Cl, F) and sulphur release during explosive, effusive, and intrusive phases of the 2011 rhyolitic eruption at Cordón Caulle volcano (Chile). Volcanica 2:73–90. https://doi.org/10.30909/vol.02.01.7390

Scott JAJ, Mather TA, Pyle DM, Rose WI, Chigna G (2012) The magmatic plumbing system beneath Santiaguito Volcano, Guatemala. J Volcanol Geotherm Res 237–238:54–68. https://doi.org/10.1016/j.jvolgeores.2012.05.014

Shea T (2017) Bubble nucleation in magmas: a dominantly heterogeneous process ? J Volcanol Geotherm Res 343:155–170. https://doi.org/10.1016/j.jvolgeores.2017.06.025

Shea T, Gurioli L, Houghton BF (2012) Transitions between fall phases and pyroclastic density currents during the AD 79 eruption at Vesuvius: building a transient conduit model from the textural and volatile record. Bull Volcanol 74:2363–2381. https://doi.org/10.1007/s00445-012-0668-z

Shea T, Hellebrand E, Gurioli L, Tuffen H (2014) Conduit- to localized-scale degassing during Plinian eruptions: insights from major element and volatile (Cl and H_2O) analyses within Vesuvius AD 79 Pumice. J Petrol 55:315–344. https://doi.org/10.1093/petrology/egt069

Shea T, Leonhardi T, Giachetti T, Lindoo A, Larsen J, Sinton J, Parsons E (2017) Dynamics of an unusual cone-building trachyte eruption at Pu'u Wa'awa'a , Hualālai volcano, Hawai'i. Bull Volcanol 79. https://doi.org/10.1007/s00445-017-1106-z

Signorelli S, Carroll MR (2002) Experimental study of Cl solubility in hydrous alkaline melts: constraints on the theoretical maximum amount of Cl in trachytic and phonolitic melts. Contrib Mineral Petrol 143:209–218. https://doi.org/10.1007/s00410-001-0320-y

Stasiuk MV, Barclay J, Caroll MR et al (1996) Degassing during magma ascent in the Mule Creek vent (USA). Bull Volcanol 58:117–130. https://doi.org/10.1007/s004450050130

Szramek L, Gardner JE, Larsen J (2006) Degassing and microlite crystallization of basaltic andesite magma erupting at Arenal Volcano, Costa Rica. J Volcanol Geotherm Res 157:182–201. https://doi.org/10.1016/j.jvolgeores.2006.03.039

Tuffen H, Dingwell DB, Pinkerton H (2003) Repeated fracture and healing of silicic magma generate flow banding and earthquakes? Geol Soc Am 31:1089–1092. https://doi.org/10.1130/G19777.1

van Wyk de Vries B, Márquez A, Herrera R, Bruña JLG, Llanes P, Delcamp A (2014) Craters of elevation revisited: Forced-folds, bulging and uplift of volcanoes. Bull Volcanol 76. https://doi.org/10.1007/s00445-014-0875-x

von Aulock FW, Kennedy BM, Maksimenko A, Wadsworth FB, Lavallée Y (2017) Outgassing from open and closed magma foams. Front Earth Sci 5:1–7. https://doi.org/10.3389/feart.2017.00046

Wadsworth FB, Vasseur J, Llewellin EW, Dobson KJ, Colombier M, von Aulock FW, Fife JL, Wiesmaier S, Hess KU, Scheu B, Lavallée Y, Dingwell DB (2017) Topological inversions in coalescing granular media control fluid-flow regimes. Phys Rev E 96:6. https://doi.org/10.1103/PhysRevE.96.033113

Wen S, Nekvasil H (1994) SOLVCALC: An interactive graphics program package for calculating the ternary feldspar solvus and for two-feldspar geothermometry. Comput Geosci 20:1025–1040

Williamson BJ, Di Muro A, Horwell CJ et al (2010) Injection of vesicular magma into an andesitic dome at the effusive–explosive transition. Earth Planet Sci Lett 295:83–90. https://doi.org/10.1016/j.epsl.2010.03.027

Wright HMN, Cashman KV, Rosi M, Cioni R (2007) Breadcrust bombs as indicators of Vulcanian eruption dynamics at Guagua Pichincha volcano, Ecuador. Bull Volcanol 69:281–300. https://doi.org/10.1007/s00445-006-0073-6

Yoshimura S, Kuritani T, Matsumoto A, Nakagawa M (2019) Fingerprint of silicic magma degassing visualised through chlorine microscopy. Sci Rep 9:1–10. https://doi.org/10.1038/s41598-018-37374-0

Zorn EU, Rowe MC, Cronin SJ, Ryan AG, Kennedy LA, Russell JK (2018) Influence of porosity and groundmass crystallinity on dome rock strength: a case study from Mt. Taranaki, New Zealand. Bull Volcanol 80. https://doi.org/10.1007/s00445-018-1210-8